REPORT DOCUMENTATION PAGE

Form Approved
OMB NO. 0704-0188

1. AGENCY USE ONLY *(Leave Blank)*	2. REPORT DATE 12/20/2000	3. REPORT TYPE AND DATES COVERED Final Report 01 Jun 95 - 30 Nov 00

4. TITLE AND SUBTITLE Multidisciplinary Research in Smart Composite Structures	5. FUNDING NUMBERS DAAH04-95-1-0104

6. AUTHOR(S)

Professors: Nesbitt W. Hagood, Stephen R. Hall, Michael Cima, Harry Tuller, Yet-Ming Chiang

7. PERFORMING ORGANIZATION NAME(S) AND ADDRESS(ES) Massachusetts Institute of Technology 77 Massachusetts Avenue, 37-327 Cambridge, MA 02139	8. PERFORMING ORGANIZATION REPORT NUMBER

9. SPONSORING / MONITORING AGENCY NAME(S) AND ADDRESS(ES) U. S. Army Research Office P.O. Box 12211 Research Triangle Park, NC 27709-2211	10. SPONSORING / MONITORING AGENCY REPORT NUMBER 33913-EG-MUR

11. SUPPLEMENTARY NOTES

The views, opinions and/or findings contained in this report are those of the author(s) and should not be construed as an official Department of the Army position, policy or decision, unless so designated by the documentation.

12a. DISTRIBUTION / AVAILABILITY STATEMENT Approved for public release; distribution unlimited.	12b. DISTRIBUTION CODE

13. ABSTRACT (Maximum 200 words)

This is the final report of the MURI program entitled Multidisciplinary Research in Smart Composite Structures. The approach taken by this program to overcome shortcomings of existing smart structures technology was that of Vertical Technology Integration. This approach has allowed the development of technology at all critical levels of functional integration, from fundamental material studies to complex controlled structures. This approach enabled a complete flowdown of applications' requirements to serve as focal points for fundamental research, and it enabled capabilities flowup to application performance which can be used as a metric to evaluate the important capabilities at each level. The research conducted by the members of this program was a coordinated effort to address issues at the materials, devices and applications levels, and the results obtained in this program represent significant steps in that direction.

14. SUBJECT TERMS	15. NUMBER OF PAGES 39
	16. PRICE CODE

17. SECURITY CLASSIFICATION OR REPORT UNCLASSIFIED	18. SECURITY CLASSIFICATION ON THIS PAGE UNCLASSIFIED	19. SECURITY CLASSIFICATION OF ABSTRACT UNCLASSIFIED	20. LIMITATION OF ABSTRACT UL

20010503 093

Table of Contents

List of Figures

List of Tables

1. INTRODUCTION

The approach taken by this program to overcome shortcomings of existing smart structures technology is that of Vertical Technology Integration. This approach has allowed the development of technology at all critical levels of functional integration, from fundamental material studies to complex controlled structures. This approach enabled a complete flowdown of applications' requirements to serve as focal points for fundamental research, and it enabled capabilities flowup to application performance which can be used as a metric to evaluate the important capabilities at each level. The research conducted by the members of this program was a coordinated effort to address issues at the materials, devices and applications levels, and the results obtained in this program represent significant steps in that direction.

According to the paradigm of Vertical Technology Integration tasks were distributed so as to address all the issues involved in improving the smart structures technology. These issues span the areas of materials, fabrication, sensing, integration, and control theory. At the level of the actuation lamina Professors Chiang and Tuller worked on the development of new active materials with improved characteristics, Professor Cima developed new fiber fabrication techniques, and Professor Hagood developed new material models to allow the investigation of more complex arrangements and the prediction of the actuation lamina behavior when damage occurs. At the Sensor/Processing lamina Professors Hagood and Hall worked on the integration of sensors and processing elements that will allow the realization of embedded actuation and sensing. At the structural level Professors Hagood and Hall have obtained important results in the areas of integral twist actuation and distributed acoustic control.

2. SUMMARY OF IMPORTANT RESULTS

2.1 GROWTH AND CHARACTERIZATION OF NEW SINGLE CRYSTAL ACTUATOR COMPOUNDS

2.1.1 OBJECTIVES

The goal of this work was to develop novel lead-free or low-lead single crystal perovskites that have the potential for high strain actuation, and to characterize their electromechanical properties. Beginning in 1997, we identified doped alkaline bismuth titanates as a promising class of perovskites suitable for growth as single crystals. These compounds typically have higher mechanical strength (2-3 times greater flexural strength), higher elastic modulus (100-110 GPa, vs. 60-70 GPa), and lower density ($\sim$6 g/cm^3, vs. 8-8.5 g/cm^3) compared to the lead relaxors (PMNPT, PZNPT). For these reasons, they are of interest as lead-free piezoelectrics which in single crystal form may exhibit attractive actuation properties for incorporation into Smart Composite Structures.

During this program, more than 50 doped single crystals were grown by the self-flux method and characterized in terms of their composition, dielectric properties, and electromechanical properties. The work initiated under this program was sufficiently promising that it was broadened in two related programs under ONR and DARPA/AFOSR support, expanding the compositional search studies into new systems, and developed new crystal growth methods with continuous growth capability such as edge-defined film-fed growth (EFG).

2.1.2 ACCOMPLISHMENTS

The Bi$_{1/2}$Na$_{1/2}$TiO$_3$- (BNT) and (Bi$_{1/2}$Na$_{1/2}$)$_{1-x}$Ba$_x$TiO$_3$ (BNBT) systems were extensively studied as prototypes for doped alkaline bismuth perovskites. Numerous flux crystal growth runs were conducted, each growth run supplying several dozen crystals of up to 2 cm diameter. The crystals were cut and polished, and their composition directly characterized using electron microprobe microanalysis. Crystal phase and lattice parameter was determined using X-ray diffraction. Actuation under uniaxial compressive stress up to 100 MPa was measured using a laser-interferometer apparatus. The results of this work have been published in the references appearing in the Appendices. The key results are summarized here:

A. We achieved the first conclusive demonstration that rhombohedral perovskite piezoelectrics as a general class undergo low-hysteresis <100> actuation. While results had existed for lead relaxors such as PMNT and PZNT, our results showed that rhombohedral phase BNT and BNBT crystals exhibit low hysteresis actuation and increase of actuation strain upon poling in the pseudocubic <100> direction, identical to the behavior of the lead relaxors. Thus the low hysteresis, fixed domain state mechanism of actuation was shown to be general to rhombohedral phase perovskites. The results were published in [1, 2].

---

1   Y.-M. Chiang, G.W. Farrey, and A.N. Soukhojak, "Lead-Free High Strain Single Crystal Piezoelectrics," *Appl. Phys. Lett.*, **73**[25] 3683-3685 (1998).

2   G.W. Farrey, A.N. Soukhojak, S. Sheets, and Y.-M. Chiang, "Growth and Characterization of Na$_{1/2}$Bi$_{1/2}$TiO$_3$-K$_{1/2}$Bi$_{1/2}$TiO$_3$-BaTiO$_3$ Single Crystal Piezoelectrics," *IEEE International Symposium on Applications of Ferroelectrics*, 24-27 Aug. 1998, Montreux, Switzerland (ISBN 0-7803-4959-8), June 1999, pp. 551-554.

(footnote continued)

B. The composition dependence of actuation in rhombohedral phase BNBT was determined. Undoped BNT was found to have $d_{33} \sim 100$ pC/N. These values increased to values as high as 650 pC/N within the rhombohedral phase field x=0 to x=0.06 (MPB composition). Strains as high as 0.25% were observed in unipolar actuation. A-site cation deficiency was then identified as a key compositional requirement for high d_{33}, as published in [3, 4].

C. An unprecedented piezoelectric strain level (0.85%) for a lead free perovskite was demonstrated, in tetragonal phase BNBT perovskite. In this composition system, tetragonal phase single crystals actuated in the [100] direction showed conventional butterfly loops characteristic of domain-switching actuation. A number of compositions showed actuation strains of ~0.4% at 30-40 kV/cm. However, one particular composition was found to exhibit 0.85% strain at 38 kV/cm (measured at 1 Hz ac field). Chemical analysis by electron probe microanalysis (EPMA) showed that this crystal had an unusually high cation nonstoichiometry with nearly 25% deficiency in the A-site cations. Single crystal X-ray diffraction showed that the crystal was of high quality and of the perovskite structure, however. These results were published in [1-4].

D. It was shown that AFE-FE field forced actuation was possible in the BNBT systems for crystals of near-MPB composition. Actuation strains of up to 0.45% were reached using this mechanism, as published in [1-4].

E. The first demonstration of edge-defined film-fed growth of a single crystal perovskite fiber in a high actuation system was made. This result was published in [3], and has lead to continuing efforts under ONR and AFOSR/DARPA support to further develop and commercialize this technology.

2.2 FABRICATION AND CHARACTERIZATION OF HIGH-STRAIN MATERIALS FOR ELECTRO-MECHANICAL ACTUATION

2.2.1 OBJECTIVES

The focus of this study is obtaining high strain actuation materials. Two approaches are considered: actuation by phase transition and piezoelectric actuation in ferroelectric materials. For the materials investigated in the $Pb(Zr_yHf_{1-y})_x,Ti_{1-x}O_3$ (PZHT) system, a phase transition between the ferroelectric (FE) and antiferroelectric (AFE) phases is induced upon the application of an external electric field. This transition is accompanied by a change of shape and volume, which can be harnessed for actuation applications. A major consideration in choosing the composition of the materials is the

---

[3] Y.-M. Chiang, G.W. Farrey, A.N. Soukhojak, S.A. Sheets, "Growth and Characterization of Alkaline Bismuth Titanate Single Crystal Piezoelectrics," Proceedings of the 9th US-Japan Seminar on Dielectric and Piezoelectric Ceramics, Nov. 3-5, Okinawa, Japan.

[4] Gregory W. Farrey, *Dielectric and Electromechanical Properties of Alkaline Bismuth Titanate Single Crystals*, S.M. Thesis, MIT, February 2000.

existence of a morphotropic phase boundary, i.e. insuring that the field necessary to induce the transition between the FE and AFE phases be temperature independent.

Recent experiments with single crystal ferroelectric materials have demonstrated strain levels of approximately an order of magnitude higher than those obtained with polycrystalline piezoelectrics. While relaxor ferroelectrics, such as $Pb(Zn_{1/3}Nb_{2/3})O_3$ - $PbTiO_3$ (PZN-PT) have been grown successfully, these lead containing materials still pose a challenge for crystal growers. The focus of our research was to find alternative, lead-free, materials for high strain actuation. Single crystal growth methods were also investigated.

2.2.2 ACCOMPLISHMENTS

PZHT phase transition actuation

PZT shows a decrease in the FE-AFE transition temperature with increasing Ti content. PHT on the other hand, shows an increase in the transition temperature with increasing Ti content (see Figure 1). By creating a PZT-PHT solid solution, one expects to achieve a morphotropic phase boundary.

The Goldshmidt tolerance factor was used to evaluate the deformation of the Perovskite structure from a perfect cube. This factor is given by:

$$t = \frac{R_A + R_B}{\sqrt{2}(R_B + R_O)} \quad \text{where } R_A, R_B \text{ and } R_O \text{ are the cation and oxygen ionic radii.} \tag{1}$$
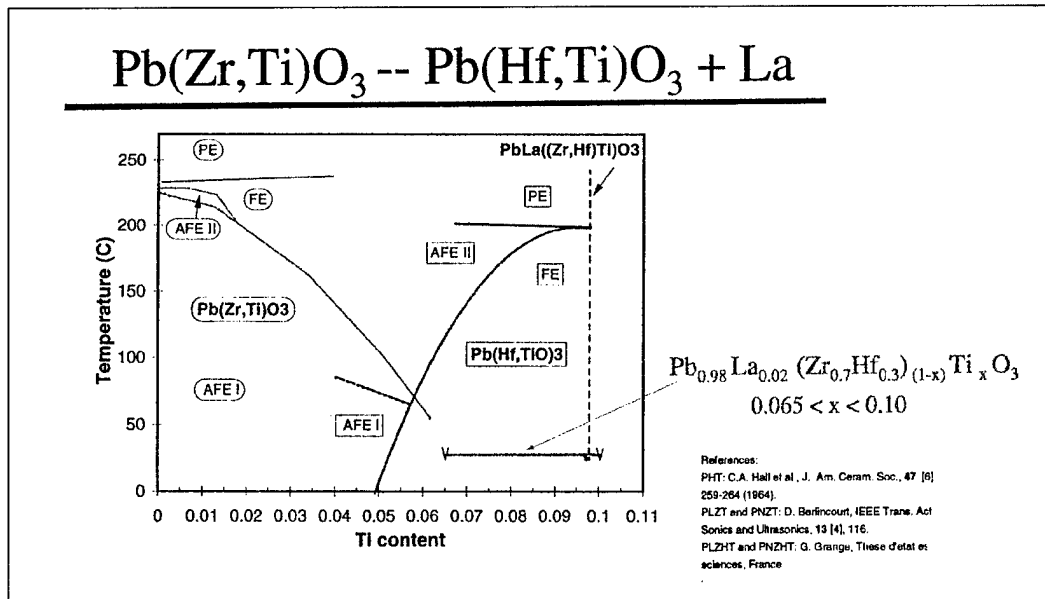
Figure 1: PZT and PHT phase diagrams — transition between tetragonal (FE) and Rhombohedral (AFE). The blue bar at the bottom right marks the compositions investigated.

By comparing the tolerance factor of PZT and PHT with various Ti concentrations, the composition for the morphotropic boundary material was estimated [5, 6]. A narrow compositional range around the optimal calculated values was fabricated and tested.

The replacement of Pb with La (~1%) improves properties such as electrical resistivity and resistance to aging and fatigue. By comparing $(Pb_{0.98}La_{0.02})Zr_{1-x}Ti_xO_3$ and $(Pb_{0.98}La_{0.02})Hf_{1-x}Ti_xO_3$ a composition of 0.7 PLZT and 0.3 PLHT was chosen, with x~0.065-0.1 (see Figure 1). These compositions showed a morphotropic phase boundary around x=0.085. By optimizing the sintering conditions, minimization of lead loss and maximization of density were obtained. Samples were prepared by solid state reaction from lead acetate and transition metal oxides. The samples were then calcined twice at 850°C to ensure full reaction and homogeneity. The reacted powders were then pressed into pellets and sintered at 1200°C in a lead rich atmosphere. Following these steps we managed a significant reduction in ZrO_2 ex-solution and a better structural integrity in the samples. This, in turn, resulted in a higher breakdown voltage and better actuation behavior.
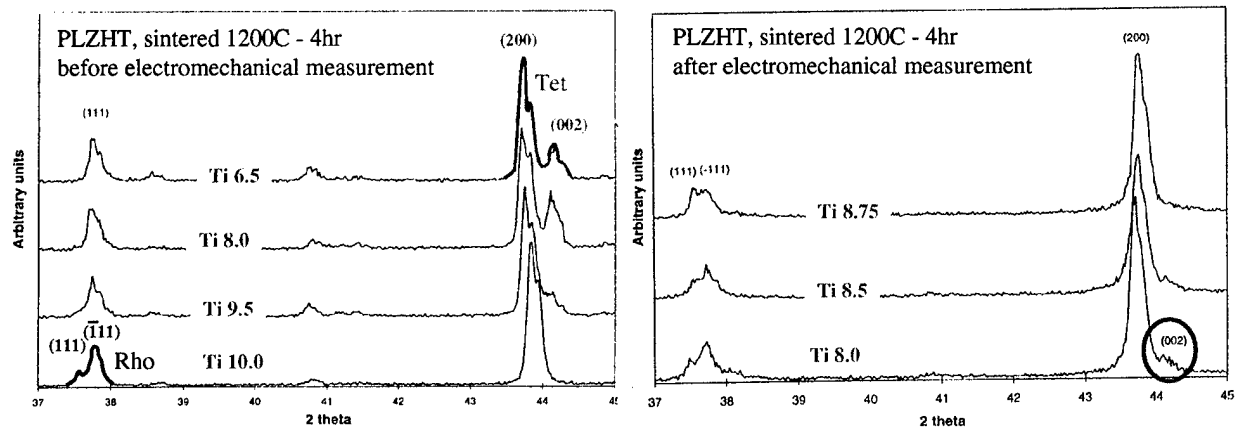
Figure 2: X-ray diffraction pattern of PLZHT showing the transition from Tetragonal at lower Ti content to Rhombohedral at high Ti content. It can also be seen that there is a region where the Rhombohedral phase is locked in after electromechanical actuation.

Figure 2 shows X-ray diffraction data of different PLZHT samples. For Ti concentration of less then 9.5%, the X-ray pattern shows a tetragonal splitting in the (200) peak, indicating the AFE phase. After electromechanical testing, samples with composition greater then 7.75% showed a transition to the Rhombohedral FE phase following electromechanical testing.

Electromechanical testing of the samples was done at different temperatures to examine actuation properties. The range of compositions investigated in this work has enabled us to confirm the existence of a nearly morphotropic phase boundary in the PZT-PHT system. Figure 3 shows the strain obtained at a field of 4 kV/mm for the composition range examined. For AFE compositions (7.75%<x≤8.5%) a high strain, relating to the AFE-FE phase transition, can be observed. The FE compositions show a much lower strain relating to the piezoelectric effect. Although the switching fields do not vary with temperature (~3.8 [kV/mm] for AFE-FE and ~0.5 [kV/mm] for reversing the process) the maximum strain varies between 0.2% and 0.3% as the temperature increases.

---

[5] C. Heremans and H. L. Tuller, Journal of the European Ceramic Society 19, 1133-1137 (1999).

[6] C. Heremans and H. L. Tuller, Journal of Applied Physics 87, 1458-1486 (2000).
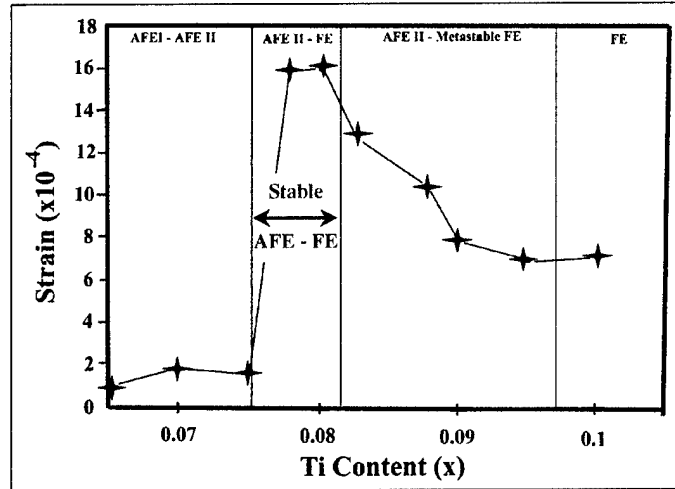
Figure 3: Strain at 4 kV/mm and the stability region of the different phases as a function of Ti content.

For the sample with Ti content of 7.75%, a maximum strain of ~0.2% was measured. The temperature dependence of the electromechanical behavior for this sample was tested and is plotted in Figure 4. It can be seen that the field required for phase transition and the maximum strain achieved are very similar for the entire temperature range.
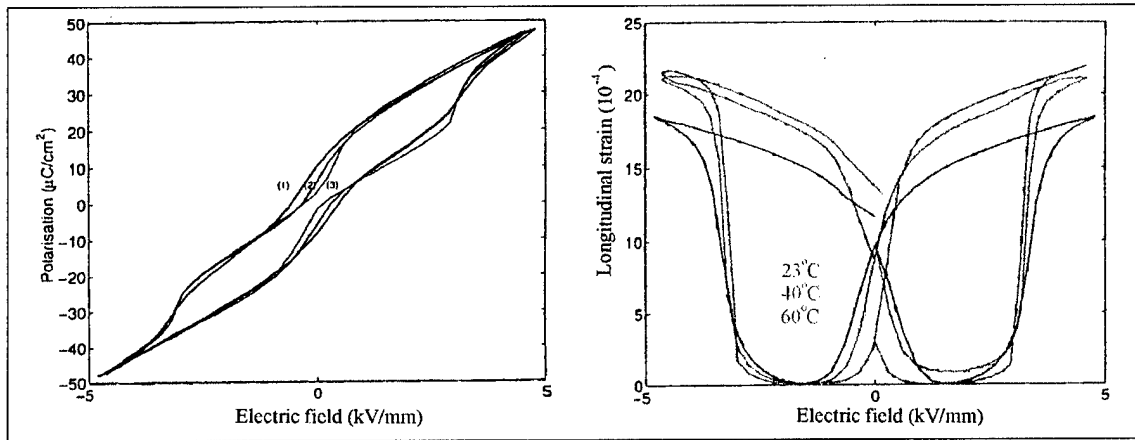
Figure 4: Strain and polarization as a function of applied field at different temperatures. The temperature insensitivity can be seen.

BaTiO₃ based actuator materials

Recent research on single-crystal relaxor ferroelectrics showed enhanced strain in the Rhombohedral phase[7]. The rhombohedral phase can accommodate a much higher strain level, especially if accompanied by a phase transition into the tetragonal phase. Although the Rhombohedral phase in $BaTiO_3$ is usually only stable at low temperatures, solid solution formation with $BaZrO_3$, $BaHfO_3$, $BaSnO_3$, and $KNbO_3$ is known to increase the stability of that phase. Polycrystalline samples were made, with various composition values in the region predicted to be Rhombohedral. These samples were tested for their piezoelectric response.

---

[7] S. E. Park and T. R. Shrout, Journal of applied physics **82**, 1804-1811 (1997).
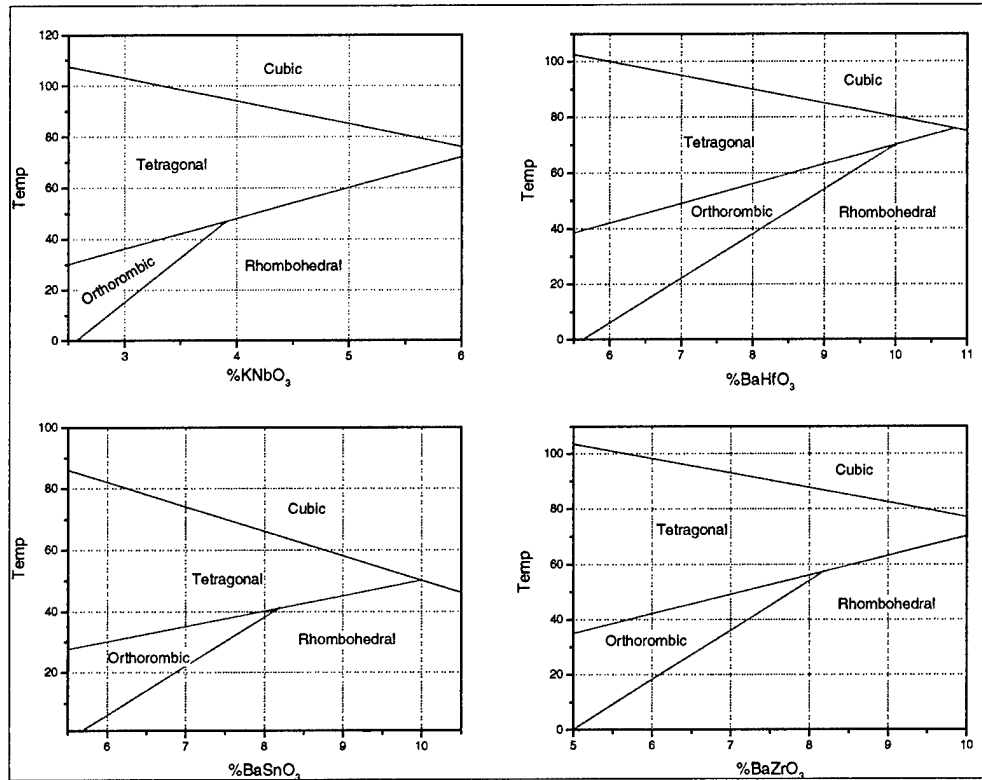
Figure 5: Calculated phase diagram for $BaTiO_3$ in solid solution with $BaTiO_3$, $BaZrO_3$, $BaHfO_3$ and $KNbO_3$. Values taken from Jaffe et. al. [8]

Samples with compositions in the range of 7-11% $BaZrO_3$, 10-11% $BaHfO_3$ and 3.8-6% $KnbO_3$ were prepared using solid state reaction of barium carbonate and transition metal oxides. X-ray measurement proved the stability of the Rhombohedral phase, as can be seen in Figure 6. The piezoelectric response for these materials can be seen in Figure 7. The results are comparable with those of polycrystalline PZT. $BaZr_{0.11}Ti_{0.89}O_3$ powders were given to Prof. Cima's group for fiber preparation. The fibers prepared were tested and found to be in the Tetragonal phase.

---

[8] B. Jaffe, W. R. Cook, and H. Jaffe, *Piezoelectric ceramics* (Academic Press, New York, 1971)
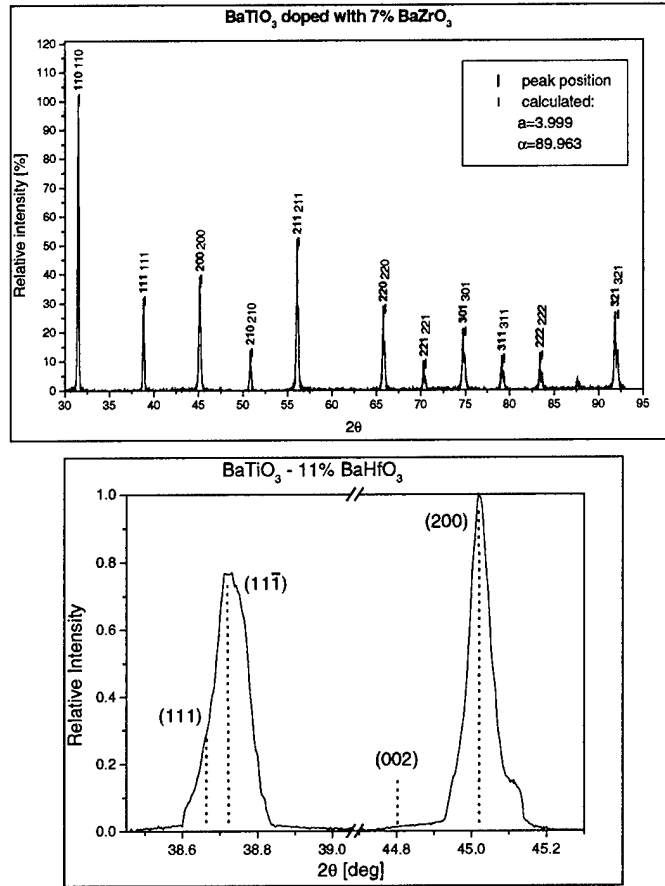
Figure 6: X-ray diffraction pattern for (a) $BaZr_{0.07}Ti_{0.93}O_3$ compared with calculations for a Rhombohedral structure and (b) $BaHf_{0.11}Ti_{0.89}O_3$ showing the rhombohedral (111) splitting.

Single crystal growth, using the floating zone method, was attempted on several compositions. The experimental setup is shown in Figure 8. A polycrystalline feed rod is melted locally using high intensity light. As the hot zone is moved up along the feed rod, crystallization occurs on the single crystal seed.

During the growth process the temperature required for maintaining a stable melt kept increasing, a phenomena associated with ex-solution of the refractive component (Zr). Although the final rod was not single crystalline, it was highly oriented with grains several millimeters long and about half a millimeter wide. Further adjustment of the growth conditions is needed in order to achieve single crystals.
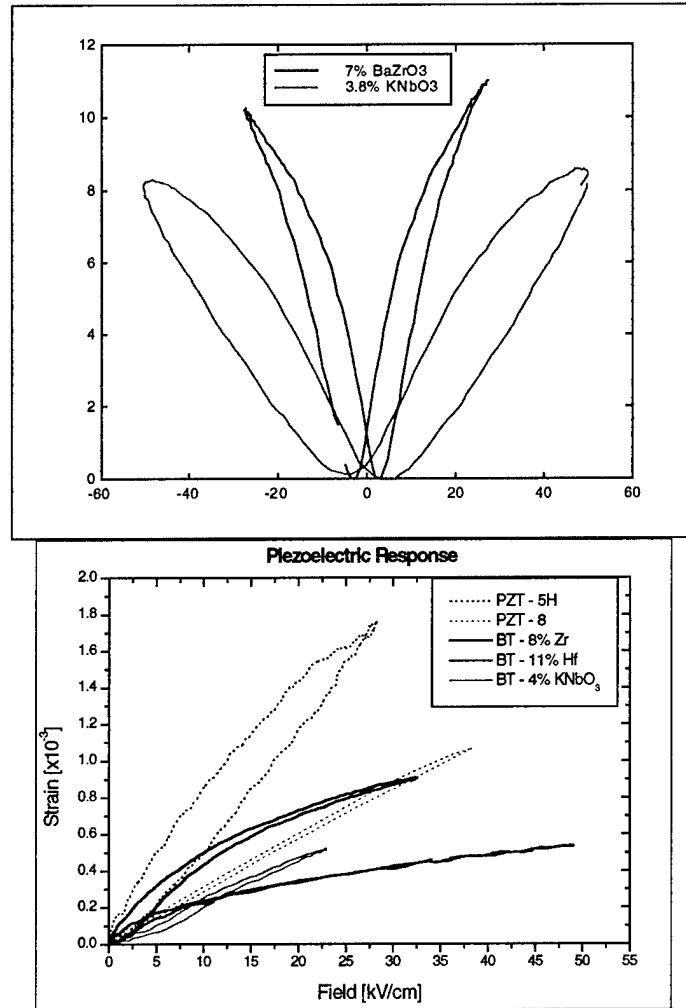
Figure 7: Strain vs. electric field curves. (a) hysteresis loop for 3.8% KNbO₃ and 7% BaZrO₃ samples (b) unipolar measurement comparing BaTiO₃ based materials with standard PZT.
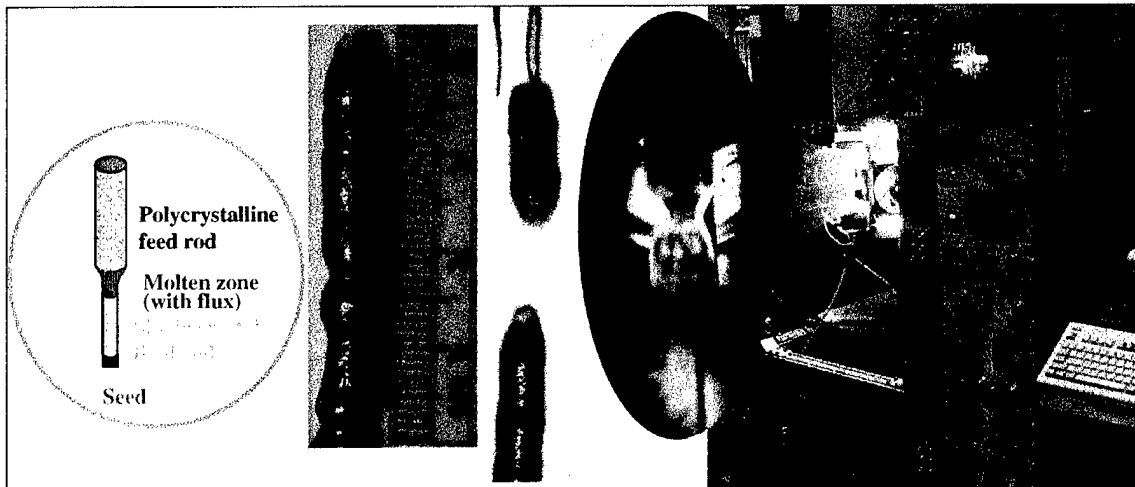
Figure 8: Experimental setup of the floating zone single crystal growth. A sample of 10% BaZrO₃ is also shown.

2.3 MICROPROCESSING OF PIEZOELECTRIC FIBERS

2.3.1 OBJECTIVES

The project objective was to develop a process for synthesizing PZT fibers for use in active composites. The approach was to fabricate re-usable micro-molds to form the fibers from a ceramic slurry. This approach was designed to allow flexibility in the batch sizes, in order to facilitate compositional studies, and also to produce denser fibers with non-uniform cross sections that could not be produced by traditional fiber production methods such as extrusion.

2.3.2 ACCOMPLISHMENTS

The development of the micromolding process is described in detail elsewhere [9]. The first step uses standard silicon processing techniques to produce a silicon master tool. A wet etch in potassium hydroxide can be used to create triangular grooves, which produce fibers with a triangular cross section. Deep reactive ion etching is used to produce fibers with a square cross section [10] Silicone rubber is poured onto the silicon tool and allowed to cure to produce a re-usable transfer mold. The silicone transfer mold can then be used to create many sacrificial wax molds. Melted paraffin wax is poured onto the cured silicone mold and allowed to solidify. It is then separated from the silicone and filled with the ceramic slurry. A rubber squeegee is used to force the slurry into the grooves in the mold and remove excess from the surface. The wax is then melted off to leave free standing green parts which can subsequently be sintered to produce the final components. The micromolding process flow is shown schematically in Figure 9.
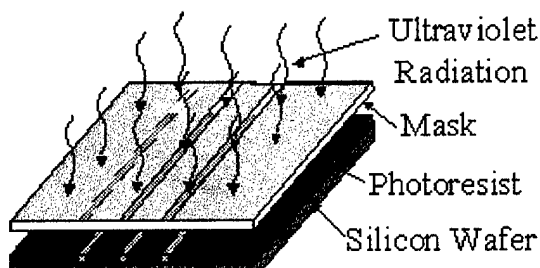
Step 1: Pattern the silicon using photolithography.

Step 2: Etch the wafer by deep reactive ion etching or wet potassium hydroxide etch.

Step 3: Pour GE RTV 31 silicone compound onto silicon mold. Allow to cure, then remove.
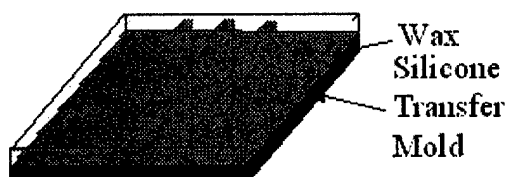
Step 4: Pour melted wax at 100 C onto the silicone mold. Allow to solidify, then remove.

---

9 Matthew E Rosenthal, "Ceramic Microforming Process" *S.M. Thesis*, Massachusetts Institute of Technology, Cambridge, MA, 1997.

10 A. A. Ayon, R. Braff, C.C. Lin, H.H. Sawin and M. A. Schmidt, "Characterization of a Time Multiplexed Inductively Coupled Plasma Etcher", *Journal of the Electrochemical Society*, 146, pp. 339-349, 1999.

Step 5: Cast ceramic slurry into the sacrificial paraffin mold and dry.

Step 6: Melt the wax off, then sinter the free-standing green parts.
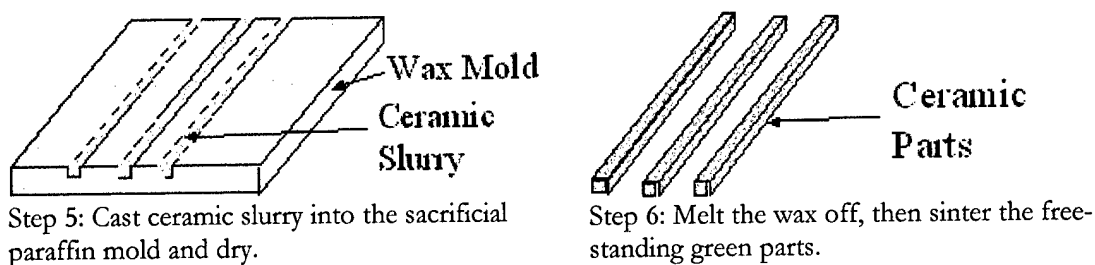
Figure 9: Schematic depiction of the micromolding process.

Fibers cast from a well-ispersed non-aqueous slurry exhibited large voids along the length, as shown in Figure 10. The formation of these voids is a result of anisotropic shrinkage during drying. The fiber begins to dry from the top surface on the mold, forming a rigid layer. The particles then cast onto this layer as the solvent continues to evaporate, leaving a large shrinkage void as illustrated in Figure 11a. This problem was solved by controllably flocculating the slurry, to reduce the shrinkage during this step as shown schematically in Figure 11b. The slurry was flocculated by adding a small amount of water to the non-aqueous formulation given in Table 1 just prior to casting. Figure 12 shows the resulting green fibers, which were free from these defects.
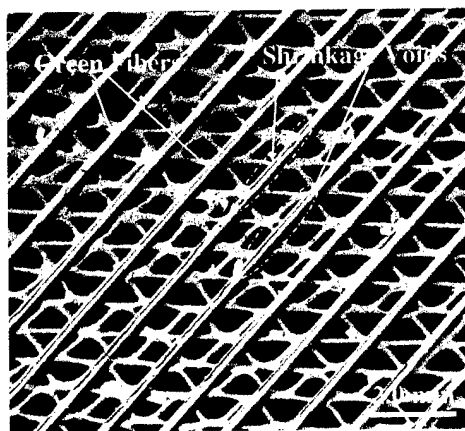
Figure 10: Shrinkage voids along the length of a fiber formed from a well dispersed slurry.

Additive	Weight Percent
PZT	85.95
Methyl ethyl ketone	10.77
Ethanol	2.64
Phosphate ester (dispersant)	0.12
Benzyl butyl phthalate (plasticizer)	0.087
Polyvinyl butyral (binder)	0.43

Table 1: Non-aqueous pzt slurry formulation.
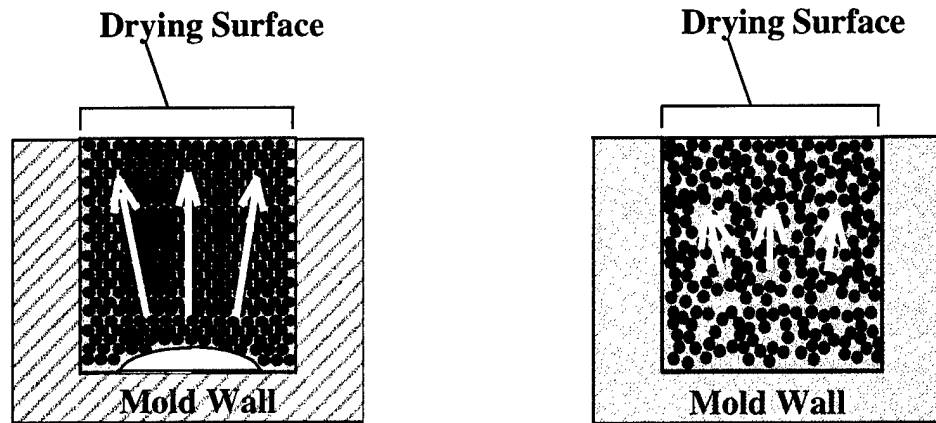
Figure 11: Schematic drawing of drying in the sacrificial mold shows a) the formation of a shrinkage void during drying of a well dispersed slurry, and b) drying of a slightly flocculated slurry.
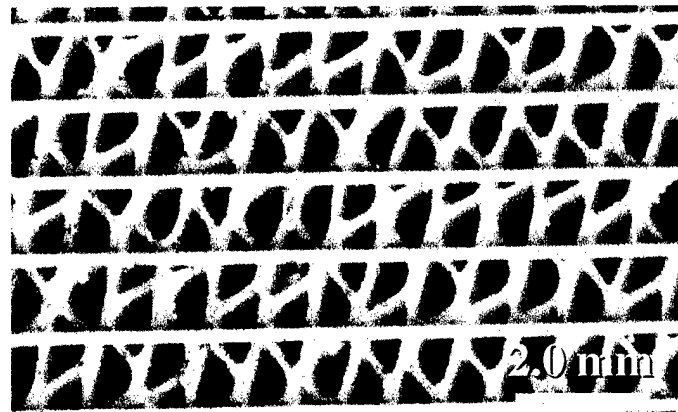
Figure 12: Green fibers formed from a slightly flocculated system showing no shrinkage voids.

A sintering technique was also developed to produce fine-grained, single phase PZT fibers. The green fibers were enclosed in a crucible surrounded by excess PZT powder to provide a lead-rich atmosphere during sintering. The fibers were sintered at 1200 C, then annealed at lower temperatures to prevent the formation of a lead oxide phase on the surface. The piezoelectric properties of the sintered fibers were measured, and showed a maximum strain of 1812 ± 170 ppm, which was comparable to that for commercial extruded fibers of the same composition, 2167 ± 493 ppm.

An active fiber composite was assembled by placing many single fibers, one at a time, into the composite structure as shown schematically in Figure 13. The poor performance and difficult assembly of the active fiber composite manufactured from these single fibers prompted investigation into arrays of interconnected fibers. These "fiber mats" could drastically simplify composite manufacture and eliminate cross-overs that degrade composite performance. A schematic drawing of a fiber mat is shown in Figure 14. Fiber mats were formed using the micromolding process described previously. Figure 15 shows a green and sintered mat. Warpage of the mat was reduced by raising the solids loading of the ceramic slurry and altering the physical design of the mats. Figure 15 shows a mat formed by this technique.
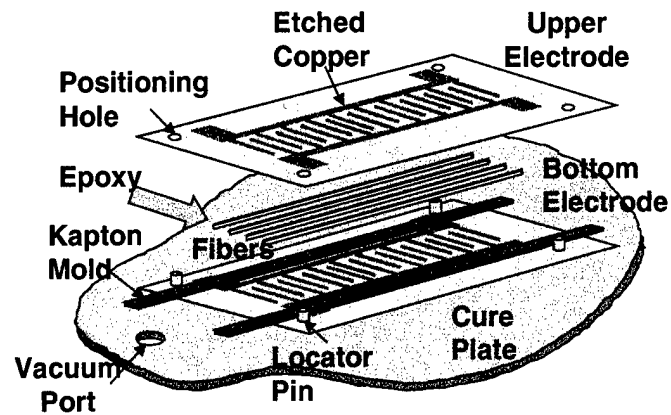
Figure 13: Schematic drawing of active fiber composite manufacture.
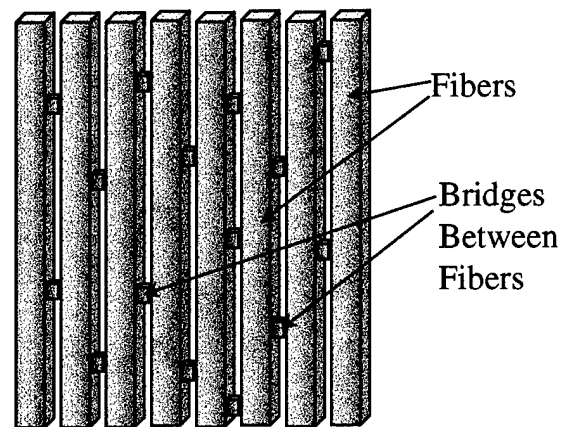
Figure 14: Schematic drawing of a fiber mat.
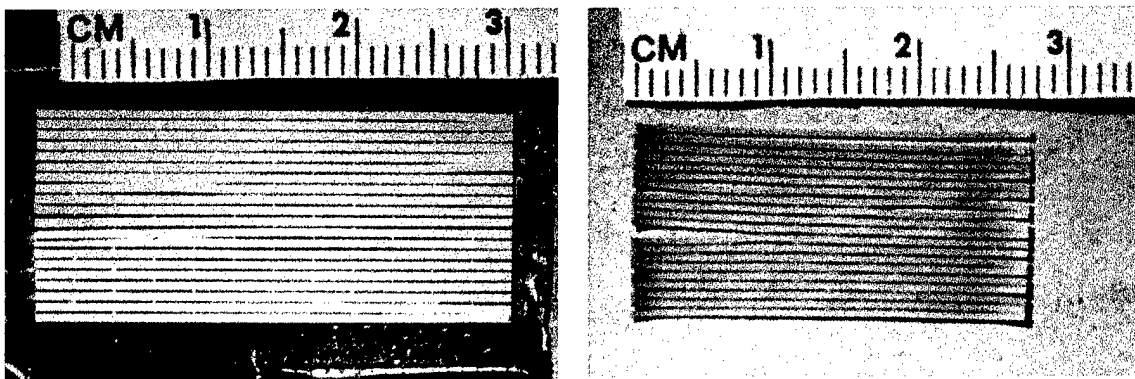
Figure 15: Photographs of a) a green fiber mat, and b) a sintered fiber mat.

2.4 DAMAGE MODELS FOR ACTIVE FIBER COMPOSITES

2.4.1 OBJECTIVES

This work aimed at characterizing and modeling the effective stiffness and actuation properties of active composite materials under high uniaxial tensile loads. The motivations for this undertaking are to obtain effective material properties as damage accumulates in the active element and to identify the mechanisms affecting stiffness and actuation to improve the material.

2.4.2 ACCOMPLISHMENTS

A unified model with predictive capability for overall laminate effective material properties was developed. Key model assumptions include a constant linear elastic fiber recovery length and a Weibull form for fiber strength. The basis for characterizing residual properties has also been established.

The model results from the integration of four separate components: Fiber Cracking Model, Effective Properties Modeling, Composite Effective Properties, and Residual Property Characterization. Issues of fiber fragmentation within the composite as a function of applied load have been addressed and a one dimensional shear lag model which was employed to characterize the load transfer between composite layers was developed. The integration of the topics mentioned above resulted into a unified model for the whole composite.

In order to validate this model several experiments were conducted on interdigitated electrode piezoelectric fiber composites embedded in E-glass laminae. Stiffness properties were determined from stress/strain data obtained from standard tensile tests. Actuation data was obtained by performing active tests: specimens were subjected to increasing tensile loads and measurements of actuation under load were taken at selected strain levels. After testing the composites were immersed in acid to dissolve the matrix material and fiber fragment counts were taken to derive key statistical parameters.

Good correlation was demonstrated between predicted behavior and experimental results. In particular, excellent correlation was demonstrated for actuation properties. In the case of actuation properties, the model captures the trend in reduced actuation as a function of increasing loads. Residual properties were also well characterized: it is now possible to predict actuation properties of composites with cracked fibers. Overall, this modeling effort is a successful and valuable step toward providing a set of new tools that will enable the production of improved active composites.

This unified model provides good predictive capability of actuation and stiffness properties of active composites. With this tool it will be possible to study the effect of various material and geometrical parameters on the composite's overall properties. This in turn will enable the development of improved active composites with the potential for a more thorough tailoring of properties for specialized applications. The findings of this work will benefit innovative applications of active composites, where the capability to predict the effects of damage will enable researchers to design more robust structures such as active helicopter rotor-blades.

2.5 INVESTIGATION OF PIEZOELECTRIC MATERIALS UNDER COMPRESSIVE AND SHEAR LOADS

2.5.1 OBJECTIVES

High compressive loads parallel to the piezoelectric material poling direction are known to depolarize these materials, while the detailed mechanism, such as time history dependency, is not yet fully understood. Analogous to compressive loads, shear loads may also have an impact on the piezoelectric material response. The objective of this work is to investigate the piezoelectric material response under shear and compressive loading with different time histories.

2.5.2 ACCOMPLISHMENTS

Compressive Depolarization

This work examined the compressive depolarization of commercial lead zirconate titanate PZT-5A piezoelectric ceramics by evaluating the actuation strain at different electric fields, compressive stresses and stress durations. Varying the combinations of these parameters allowed further understanding of the coupling effects among them. The experimental results showed a remarkable difference between the under-load actuation and the residual actuation, determined at zero stress after exposure to compressive stress. Under-load actuation was little reduced at high compressive stress either at low or high electric excitation levels and was found to be relatively independent of stress duration, while high electric drive residual actuation was found to be strongly dependent upon stress duration and maintained its initial actuation for short compression duration. The data also indicate that the compressive stress combined with high negative electric field can expedite the depolarization of material. In summary, this work provides a reference guide for designing any active device under high compressive load.

Piezoelectric Shear Test

The goal of this work is to characterize the response of the piezoelectric material under shear loading. As shown in Figure 16, the concept of the shear test is to apply a torque on a circularly polarized tube illustrated in Figure 17a. By actuating an electric field along the longitudinal direction, one can generate a shear motion of the circularly polarized tube. By applying a weight through the sheave at the end of the shear tester, one can control the shear loading on the tubular specimen. By doing so, one can therefore characterize the shear response of piezoelectric material as a function of the electric field and the shear stress:

$$S_{13} = f(E_1, T_{13}),$$
$$D_1 = f(E_1, T_{13}).$$
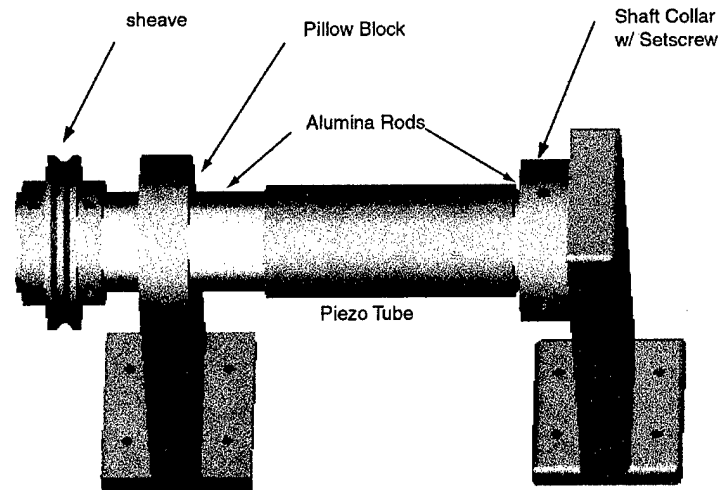
Figure 16: Shear Tester for Piezoelectric Tube

The difficulty of this work is to polarize the tubular specimen circumferentially. A continuously polarizing technique demonstrated in Figure 17b has been tried to overcome this problem. Two pairs of long electrodes are stationed at the base of the poling device, as illustrated in Figure 18a. By rotating the tubular specimen using a stepping motor, which can control the rotation and the speed, one should be able to keep the specimen being polarized along the circumference. Unfortunately, this technique failed to polarize the specimen and the specimen fractured as presented in Figure 18b. The induced polarizing stress accounted for such fracture mechanics. As shown in Figure 17b, the short section between electrodes was expanded by the polarizing electric field. This expansion resulted in a large stress in the specimen and therefore the specimen fractured.

a)   b)
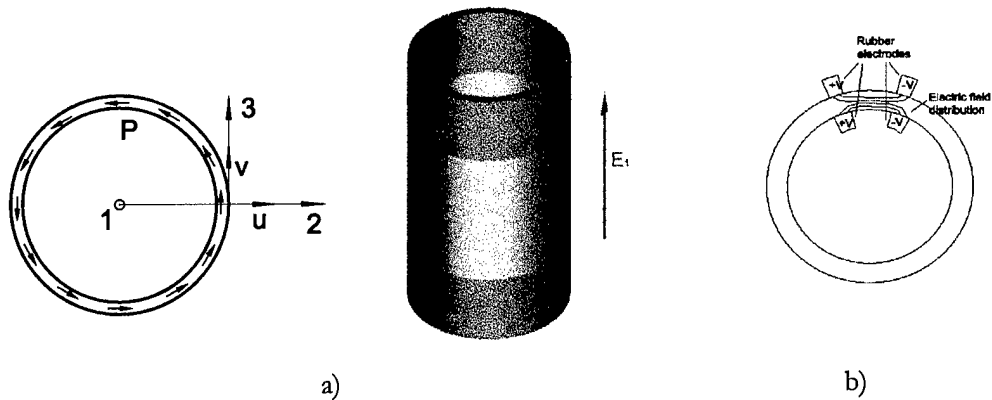
Figure 17: a) Circularly polarized piezoelectric tube; b) Electrode pairs

a)   b)
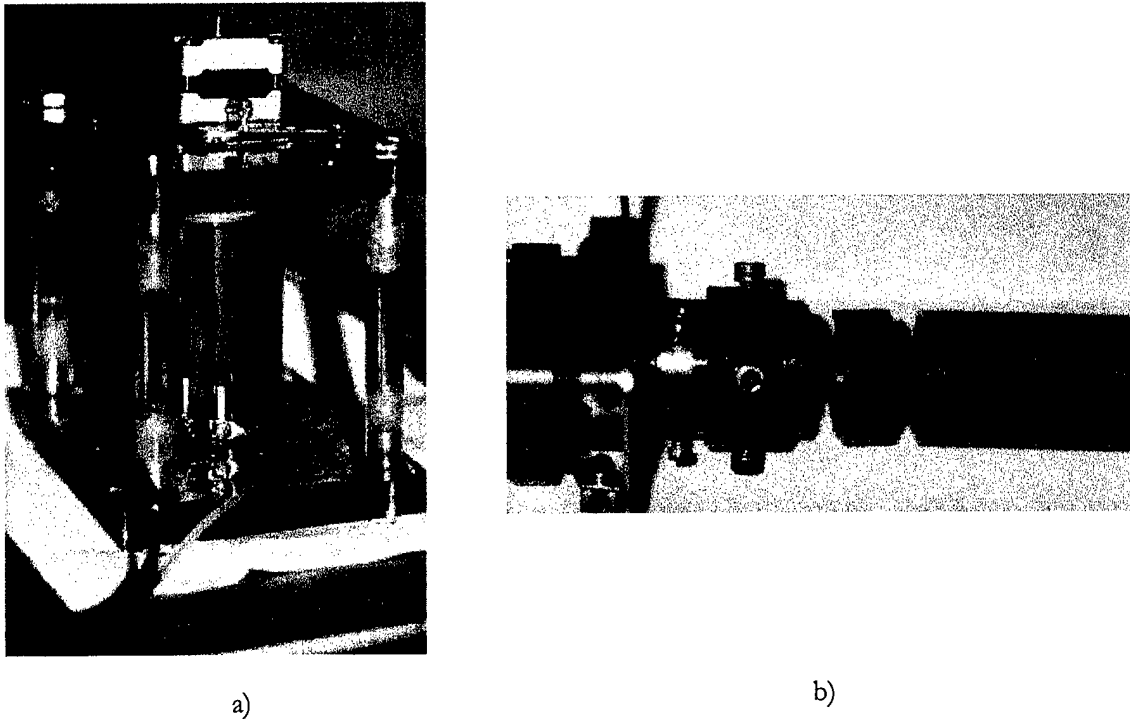
Figure 18: a) Poling device consists of two pairs of electrodes and a stepping motor; b) Specimen fractured after being polarized.

2.6 FINITE ELEMENT MODELING OF PHASE TRANSITIONING MATERIALS

2.6.1 OBJECTIVES

The objective of this study was to develop a finite element approach for modeling the nonlinear behavior of electro-mechanically coupled materials. The approach can model repolarization in ferroelectrics (PZTs) as well as ferroelectric-antiferroelectric phase transitions in electroceramics (e.g. PbLaZrSnTi, or PHZT systems). Finite element models formulated with this element can be used to analyze response of material systems with complex geometries such as interdigitated electrodes and piezofiber composites under high applied electric fields, which produce nonlinear response.

2.6.2 ACCOMPLISHMENTS

A 3D nonlinear material model capable of modeling repolarizations in ferroelectrics (PZTs) has been formulated. It is derived from an expansion of the energy in terms of tensor invariants of strain and electric displacement. The polarization vector is also included as an internal variable in the expansion along with a transition criteria which allows modeling repolarization behavior of ferroelectrics. Nonlinear response of PZT-5H blocks was characterized experimentally under a host of electrical and mechanical loading conditions, and used to determine the parameters in the material model. The model produces strain and electric displacement hysteresis loops observed in the material, and captures both the electric field and stress dependence of these curves.

The nonlinear material model is incorporated in a nonlinear finite element formulation to allow analysis of complex devices. A three-dimensional 4 node mixed element has been formulated using a

novel variational principle. In addition to nodal displacement and voltage degrees of freedom used in conventional coupled elements, the mixed element also utilizes internal electric displacement degrees of freedom, resulting in significant improvement in numerical efficiency. Numerical stability of the mixed element formulation has been examined, and a corresponding inf-sup criteria has been established.

A major accomplishment has been the experimental characterization of nonlinear properties of PZT-5H. The experiments consisted of measuring the response of piezoelectric samples under a combination of mechanical and electrical loading conditions. Simple finite element runs using a commercial package were used to determine the minimum aspect ratio required for the samples to ensure uniform fields. Based on these results a samples size of 0.25" x 0.25" x 0.75" was selected for the experiments. Four or five gages were mounted on each sample to measure the strain in the different directions. Redundant gages were used to insure the samples were uniformly loaded.

Each sample was subjected to a sinusoidal voltage, while under constant transverse or longitudinal mechanical load. The strains in different directions and the electric displacement were measured during each test. In this manner, electric displacement-electric field hysteresis loops as well as strain-electric field butterfly curves were obtained under different mechanical loading conditions. From this data, it is possible to see how a compressive load in the longitudinal or transverse direction effects the polarization behavior of the material. While a compressive load transverse to the electric field direction has minimal effect on the shape of the electric hysteresis loop, a compressive longitudinal load significantly changes the shape of the hysteresis curve. Corresponding changes in the strain-electric field butterfly curves were also observed, which the material model attempts to capture.

The data obtained from the material characterization experiments was used to specify the parameters in the material model. The quadratic cost function was defined in terms of the error between model and experimental data. Minimization of this metric with respect to model parameters produced an optimal value for the parameters. The resulting material model was observed to capture the trends in the high field nonlinear response of the model over a wide range of mechanical loading conditions. The material model was then incorporated into the nonlinear finite element code. Experiments were also performed which were designed to validate the finite element model (Figure 19). Specifically, model predictions were compared to macroscopic deformations observed experimentally in a sample with nonuniform electric field and polarization distribution. The correctness of the solution obtained with the mixed formulation was validated (Figure 20).
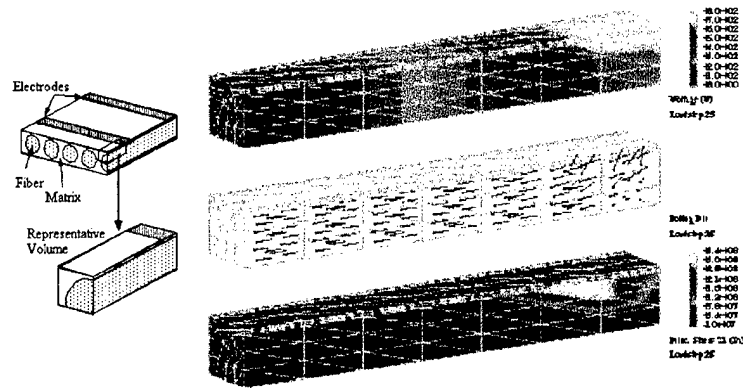
Figure 19: Finite element mesh of an interdigitated piezofiber composite.
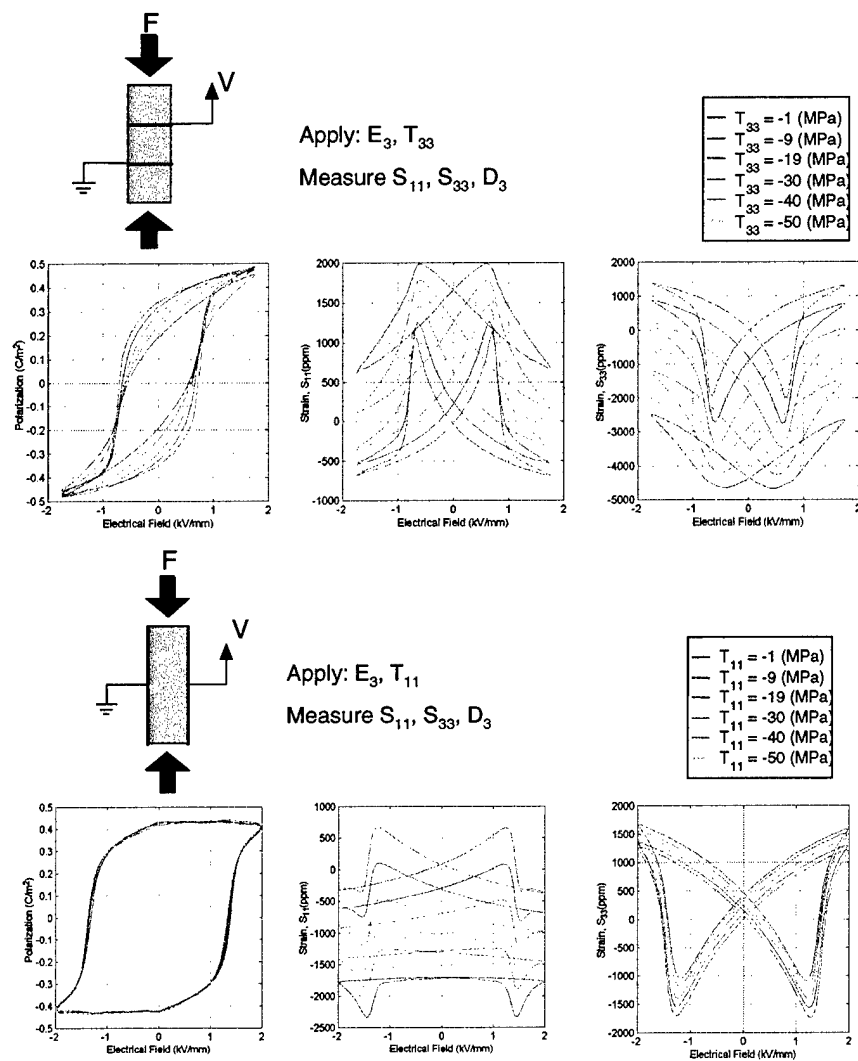
Figure 20: Experimental and theoretical curves for different loading conditions.

2.7 NONLINEAR PIEZOELECTRIC SHUNTING FOR PASSIVE STRUCTURAL DAMPING

2.7.1 OBJECTIVES

The goal of this work was to examine the use of nonlinear shunting circuits to yield electro-mechanical systems with damping levels greater than those with conventional linear shunting (resistive, tuned resonant). Increases in damping levels could provide improved performance in systems where vibration disturbances cause loss in system accuracy, or reductions in structural lifetimes and reliability. Other strong motivations for nonlinear approaches to shunted damping include reduced sensitivity to frequency tuning and recovery of the vibrational energy in usable electrical form for powering other devices.

2.7.2 ACCOMPLISHMENTS

Figure 21 illustrates the circuit equivalent diagram of a passively shunted single mode structure. PZT based materials bonded to/embedded in structures act as a transduction path, converting mechanical energy (from the motion of the structure) to electrical energy. This PZT element is connected to shunt electronics. The shunt electronics can consist of multiple components, such as a rectifying bridge to direct energy away from the structure, and energy storage. Energy can be stored in one of a number of ways, including a capacitor, DC voltage supply, or other storage element. Optimization of the shunt circuitry maximizes energy removed from the structure, and power available to other devices.
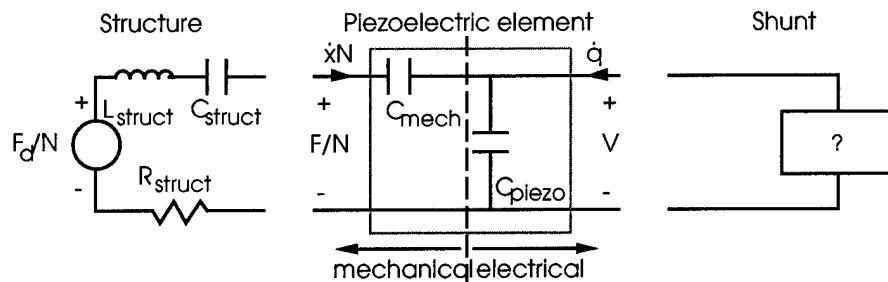
Figure 21: Generalized electrical equivalent network for shunted PZT element coupled to resonant structure.

A basic framework for analysis of nonlinear shunting has been developed which allows comparison of the effectiveness of different shunting designs. The method applies electro-mechanical modeling of equivalent circuit elements to determine the effective material loss factor, based on the conventional definition of system energy flow and loss.
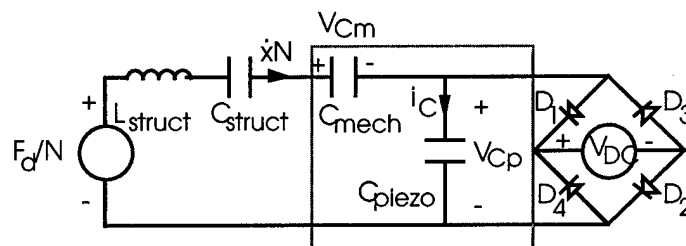
Figure 22: A possible realization of nonlinear shunted network: rectified DC voltage source.

The analysis has been performed for several concepts, one of which is shown in Figure 22. In this case, the PZT has been shunted to a rectified DC voltage source, possibly representing a rechargeable battery or regulated switching power circuit. The shunt voltage is assumed to be

constant; when the voltage across the piezoceramic is lower than that of the shunt, no current flows to the DC source, and the PZT exhibits open circuit behavior. When the piezoceramic voltage reaches the shunt voltage, current flows and the PZT behaves as if short circuited, but with an offset which appears in the force-displacement diagram (Figure 23a) as a preload. Because the preload depends on the direction of current flow, it appears positive and negative over different parts of the cycle. The area of the resulting hysteresis loop represents energy *delivered* to the DC shunt element.
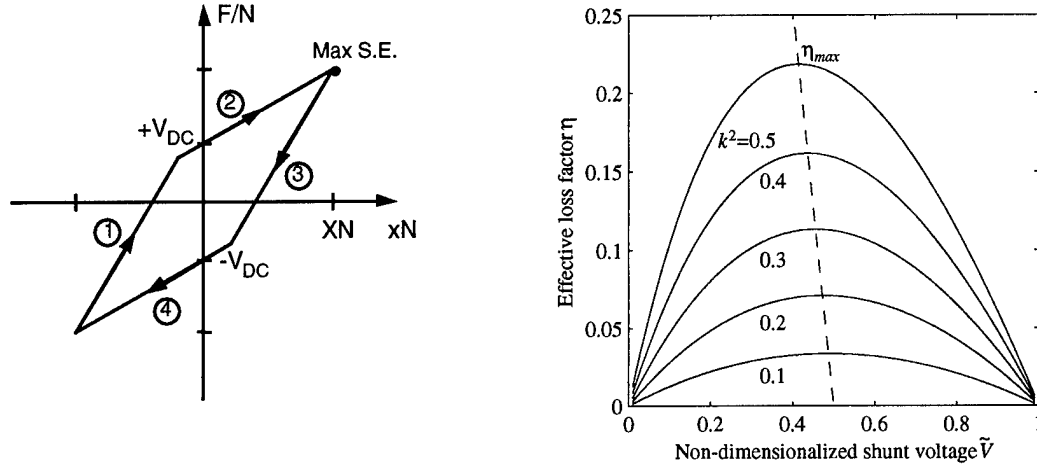
Figure 23: Results of electro-mechanical modeling of rectified DC source shunt. (a) Hysteresis curve in equivalent force-displacement plane, caused by open and short circuit conditions on PZT, (b) Design curve, illustrating effective loss factor as a function of the non-dimensionalized shunt voltage.

A comparison of the energy removed over one cycle to the maximum energy stored (in mechanical strain energy), forms the definition for the material loss factor. This results in design curves for the effective material loss factor as a function of the PZT coupling coefficient, and the non-dimensionalized shunt voltage (Figure 23b). The actual optimal shunt voltage further depends on the amplitude of vibration. Typical values for the material loss factor of PZT are 0.38, operating in transverse mode, and 0.75 operating in longitudinal mode (for a $k^2 \sim 0.56$).
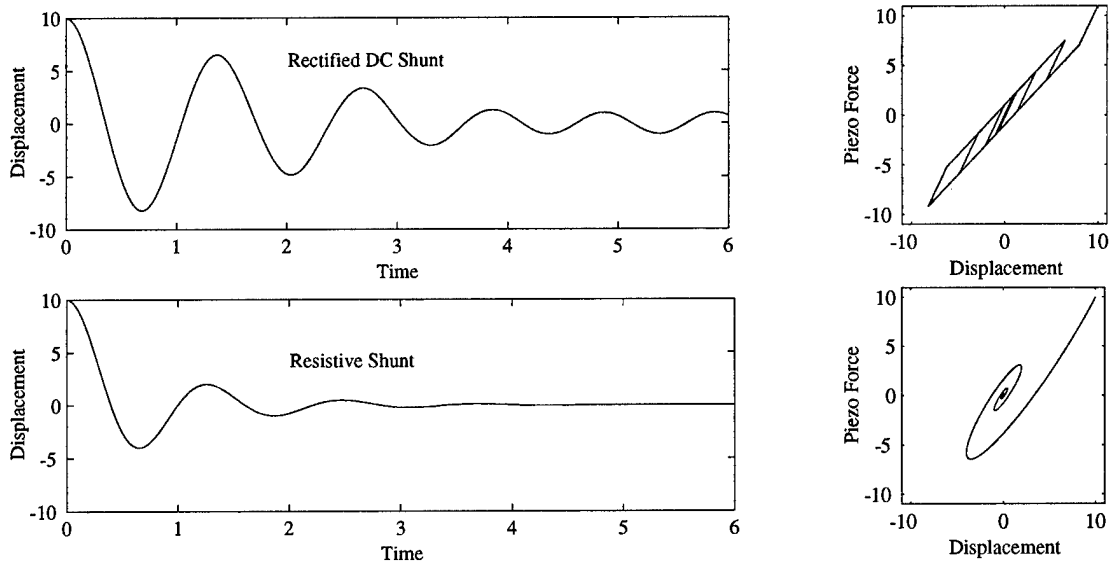
Figure 24: Results of numerical simulation of single mode structure coupled to shunted PZT network. Top: Rectified DC voltage source shunt, Bottom: Conventional resistive shunt, ideally tuned.

For application to a resonant system, the formulation is easily modified by coupling the PZT and shunt components to the electrical equivalent network for a structure, as shown in Figure 21. The mass and compliance of the system are represented by the structural inductance and capacitance, respectively, and the applied external force is represented by an equivalent voltage source. The *effective* material loss factor now represents both the PZT and structural coupling, due to the new equivalent capacitance (mechanical compliance). Numerical simulation of the resulting network equations demonstrate the *damping* caused by the rectified DC voltage source network (Figure 24). Although a purely resistive network (ideally tuned to the structural mode) gives somewhat larger damping ratios than for this particular nonlinear shunt network, the damping of the nonlinear shunt is available to all structural modes. Furthermore, useable energy from the structure is recovered and stored.

This work represents a novel approach to passive shunted damping techniques for dynamic structures. The groundwork laid allows the assessment of future nonlinear shunting schemes for effectiveness of design. In particular, variable resistor and adaptively varying DC voltage sources show promise for substantially higher damping levels than conventional resistive shunting. Practical circuit realizations of the network components will also be developed, including miniature and embeddable realizations.

2.8 TECHNOLOGIES FOR EMBEDDED SENSOR AND ACTUATOR ARRAYS FOR SMART COMPOSITES

2.8.1 OBJECTIVES

The objective of this research was to demonstrate a smart composite structure utilizing arrayed embedded sensors and actuators. The construction of a smart composite requires three separate technologies: manufacturing of embedded sensors and actuators, onboard signal conditioning and communications, and hierarchical processing of the information. The resulting smart structure would be able to sense damage, estimate shape, and actively damp structural vibrations. This study focused on the first technology listed above.

2.8.2 ACCOMPLISHMENTS

Manufacturing, data processing and control issues must be addressed in order to accomplish sensing and control of a smart structure. Embedding sensors and actuators into a composite is the first step toward creating a smart structure. Of primary concern is developing a strategy to embed the electronics without shorting to the carbon fibers. On thin sensors and actuators, such as strain gages and AFCs (active fiber composites), this can be accomplished with the use of Kapton. For larger components such as pressure gages and accelerometers, more elaborate schemes are required. To help shield the sensors from electromagnetic interference a ground plane can be embedded as well, such as copper coated Kapton.

Getting the signal information off of the composite panel is an issue that needs to be addressed. Micro-sensors tend to have low output power, and the signal is badly attenuated with high signal noise in a relatively short distance. So signal conditioners and amplifiers must also be embedded. Additional problems are created by having a large number of sensors. This requires creating a bus structure and switching architecture to handle the large number of signals. The bus structure is also beneficial by reducing the count of wires leaving the panel.

The third aspect of smart composite design is creating an algorithm to interpret the data signals. Accelerometer and strain data can be combined to estimate the shape of a structure. The

accelerometers pick up the higher frequency vibrations and the strain gages are used to pick up the lower frequency and quasi-static deformation.

Experiments were conducted to determine what effect the actuator's high electromagnetic field had on the embedded sensor. The experiment consisted of manufacturing and running closed-loop experiments on a composite laminate with active fiber composites (AFCs) actuators and foil strain gauges sensors.

The basis for the composite laminate used as the structural-acoustic testbed is a quasi-isotropic layup typical in applications which benefit from the increased stiffness and strength to weight ratio of composite structures. A quasi-isotropic laminate has equivalent extensional stiffness in the two in-plane directions and no bend-twist coupling. For this panel an eight-ply symmetric layup, denoted by $[0/\pm45/90]_s$ of graphite/epoxy (AS4/3501-6, 32% resin, from Hercules Inc.) is used as the nominal passive layup. The dimensions of the panel, 10.3x12", are chosen to have dynamic response similar to a single panel of a typical commercial aircraft or rotorcraft. To accommodate the embedded sensors and actuators and provide a measure of electrical isolation, three e-glass host plies (450-1/2 glass fabric with F155 resin system - Hexcel Corporation) were incorporated into the lay-up for each active ply. A ply the full size of the panel was included both above and below the two active layers while material was removed from the middle layer of e-glass in order to incorporate the AFC's with minimal thickness discontinuities. The full lay-up is illustrated by the typical cross-section shown in the Figure 25.
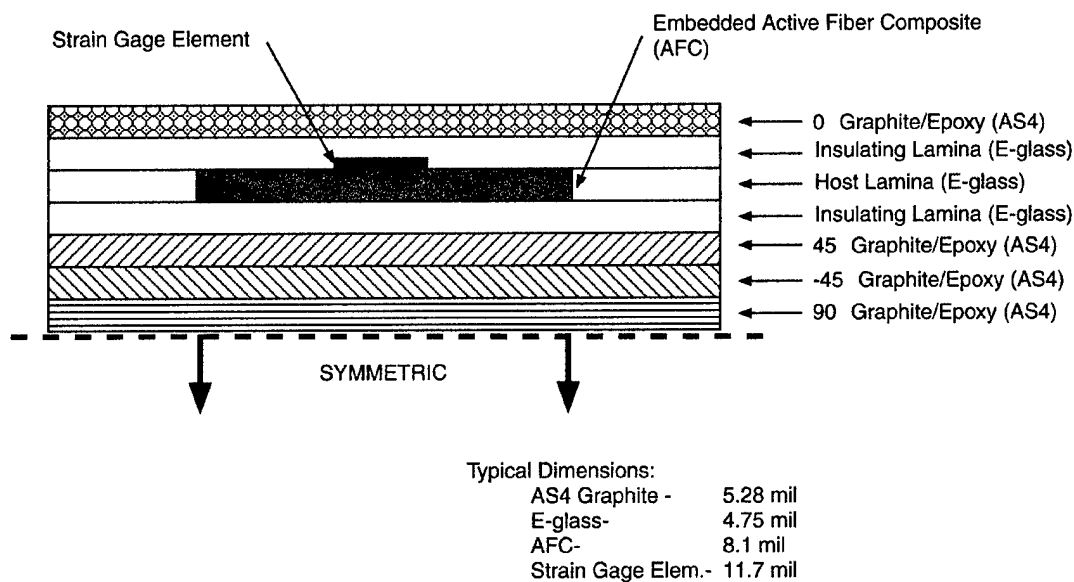
Figure 25: Layup of composite structural-acoustic test panel.

Three issues are critical for incorporating structural sensors and actuators into laminate structures: isolation, shielding, and connections. Active fiber composites (2"x3" AFC's from MIDE; Cambridge, MA) require very large driving potentials, demanding that the power leads be well insulated from the surrounding conductive graphite plies. Kapton encapsulated flexible circuits (AllFlex) were placed between the composite plies to minimize the discontinuities. Strain gage sensors $(0/90^{\circ}$ T-Rosettes from Measurements Group - CEA-06-062UT-120) are very sensitive to electro-magnetic field disturbances, such as the high electrical fields from the AFC's, and require proper shielding in order to accurately measure strain. Finally each of the elements must be robustly connected when

assembling the pre-preg laminate in order survive the harsh environment of a composite cure (e.g., 350° F and 85 psi).

Figure 26 shows the positioning of the embedded elements in the composite test panel. The interdigitated electrode pattern is shown on the individual AFC elements and the fiber direction is perpendicular to the electrode lines. Each of the actuator pairs is placed symmetrically about the neutral axis at the indicated locations and electrically connected 180 degrees out of phase to produce a bending moment. The embedded strain sensors successfully measured the strain at the locations under piezoelectric actuation, but were not used in the closed-loop experiments.
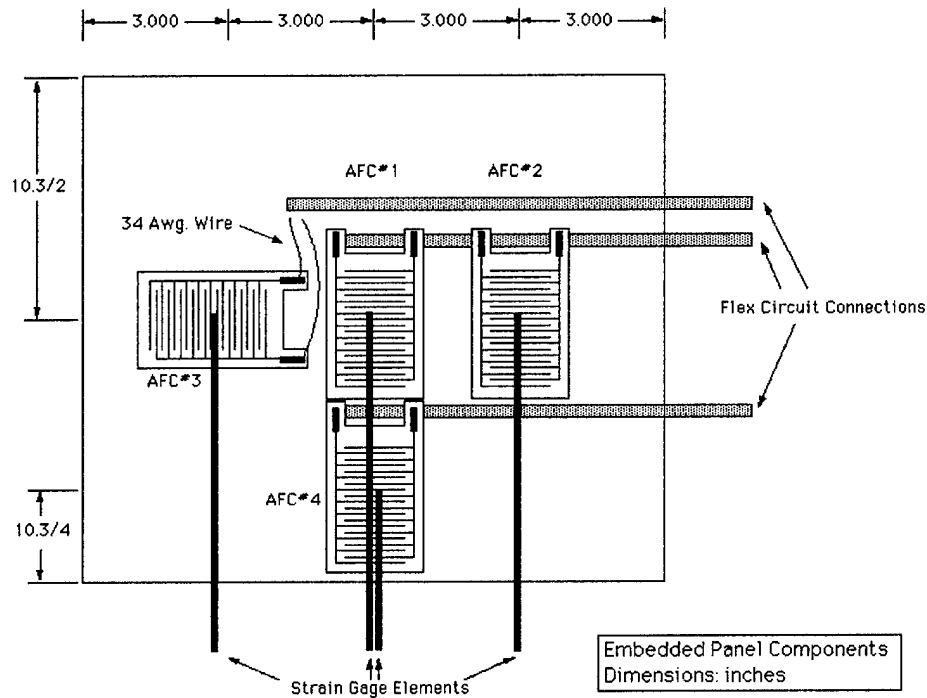
Figure 26: Layout of AFC's in structural-acoustic test panel.

The successful embedding of actuators and sensors into the composite structure is the first step toward the creation of a smart composite. Being able to shield the sensors from the electromagnetic interference is also of considerable significance. This allows the sensors to be placed in greater proximity to actuators and other sources of electromagnetic interference, while ensuring a good signal output. Having the sensors collocated with the actuators in turn increases the controllability of the structure.

2.9 DISTRIBUTED STRUCTURAL ACOUSTIC CONTROL

2.9.1 OBJECTIVES

This study focused on the application of active materials to the problem of controlling the interior acoustics and skin vibration of a fuselage test-bed. Issues addressed during the program were: the design, modeling and construction of a test-bed representing a typical helicopter fuselage, a detailed control analysis on a two-dimensional model, the choice of sensors and actuators, investigation of methods that would simplify bonding, and ways to increase the performance of the actuators in order to have control authority over a wider frequency range.

2.9.2 ACCOMPLISHMENTS

A fuselage test-bed was used in this research to study active structural-acoustic control techniques. The fuselage (Figure 27) consists of a skin made of 0.762 mm thick aluminum, riveted onto a framework of six ribs and 12 stringers. The fuselage is cylindrical in shape, with rounded end caps. The end caps are constructed of thicker aluminum, without an underlying frame, to simplify construction. Although not a scaled model of an actual aircraft fuselage, the test-bed was designed using a hybrid scaling technique, to have many of the features of full-size fuselages. Because the model fuselage has fewer ribs, stringers, and panels than a full-size fuselage, geometric scaling of typical components would not result in realistic dynamics. To get the most realistic dynamics possible, the stiffnesses of individual ribs and stringers were made greater than would be predicted by geometric scaling, so that the overall bending stiffness of the fuselage scales properly. Likewise, the panels are thicker than would result from a geometric scaling, so that their natural frequencies are close to the (scaled) natural frequencies that would result from a true geometric scaling.
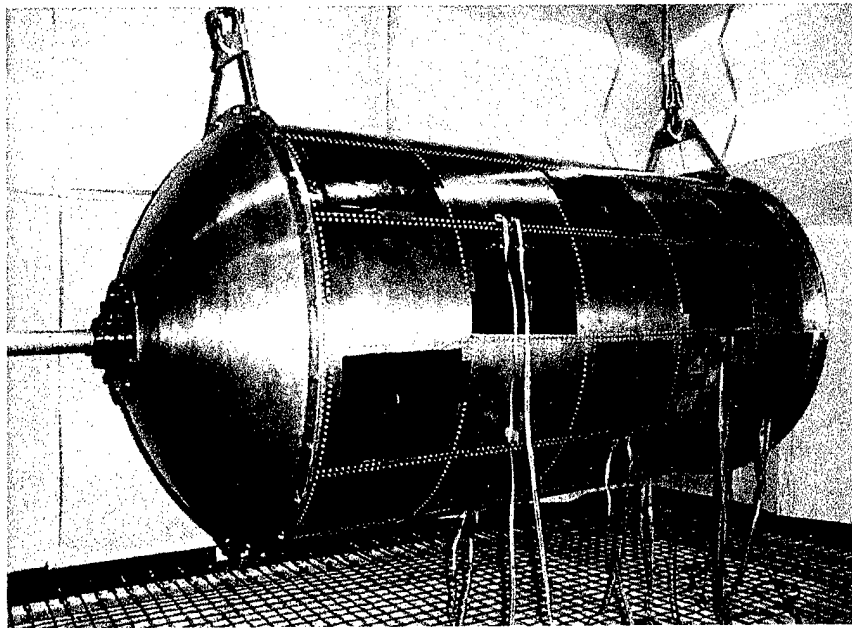
Figure 27: The fuselage test-bed instrumented with active plies.

Even though the test-bed is less complex than a full-scale fuselage, it is still very complex, with hundreds of modes in the bandwidth of interest. Therefore, it was not possible to develop an accurate structural-acoustic model of the test-bed. A two-dimensional model of a generic cross-section of the test-bed was used to evaluate possible choices of type and location of sensors and actuators. Based on his results, it was concluded that collocated rate feedback is the most desirable control method for damping structural modes over a broad frequency range. Piezoelectric ceramic actuators collocated with PVDF (polyvinylidene flouride) sensors were chosen as sensor-actuator pair. The actuators used in this research are PZT (Lead-Zirconate-Titanate) 5A wafers, with dimensions 63.5 mm x 63.5 mm x 0.254 mm manufactured by Morgan-Matroc. The PVDF sensors are collocated with the actuators, and have dimensions 63.5mm x 63.5 mm x 0.0508 mm and were manufactured by MSI.

Figure 28 shows the configuration of the active plies used in this experiment. Each active ply has two layers: the sensing layer and the actuation layer. The actuation layer has 5 PZT patches bonded between two layers of copper-coated kapton. Each copper layer was etched to form an electrode pattern. The sensing ply was prepared in the same manner, using PVDF film instead of PZT. The sensing ply was bonded to the top of the actuation ply with epoxy to form a single active ply. A layer of copper-coated kapton was sandwiched between the sensing and the actuation plies to serve as a shield against capacitive coupling. Each active ply was bonded to the structure with 3-M thermoplastic. Thermoplastic adhesive was used to allow easy removal of the active ply in case it became necessary to replace one of the plies.

Figure 28: Lay-up of the active ply with PZT actuators and PVDF sensors.

In addition to the PZT actuators and the PVDF sensors, accelerometers were mounted to the surface of the fuselage, to allow direct measurement of the panel motion. These measurements provide an indirect measurement of t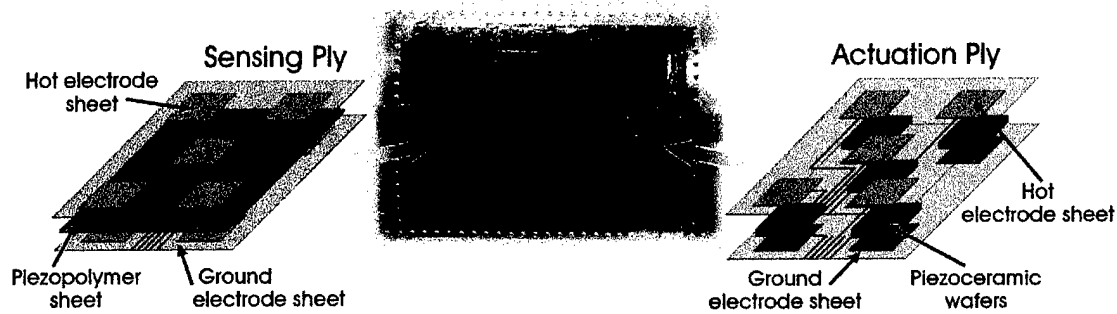he performance of the closed-loop controllers. Finally, an array of microphones in the interior of the fuselage provides a direct measurement of the reduction in noise levels provided by feedback control.

The closed-loop experiments were performed by exciting the disturbance PZT patch with 0--2~kHz random noise generated by a personal computer connected to a Siglab digital signal processing system. The performance of each controller was measured using accelerometers and microphones. One accelerometer was attached on the inside of each fuselage panel that is instrumented with an active ply.

Broadband Feedback Control

In designing the control laws, the main goal was to damp structural vibration, especially of the panels, over a broad frequency range. This should reduce the interior noise levels, because most of the noise in the interior is radiated by the panels, which couple well with the interior acoustics. The simplest approach for damping vibration in a structure with collocated sensors and actuators is often rate feedback, because it usually guarantees stability. However, in this case, rate feedback does not work, because the resulting loop gain does not roll off with increasing frequency. This is a general result - whenever a collocated pair consists of an applied stress actuator acting in bending, and a strain actuator sensing strain rate, the backbone of transfer function will slope upwards at high frequencies. To address this problem, it becomes necessary to use a controller transfer function that applies rate feedback up to a desired frequency, and then rolls-off for gain stabilization. The control law used has the form of a second order system,

$$K(s) = \frac{k\omega_n s}{s^2 + 2\zeta_n \omega_n s + \omega_n^2},$$

where ω_n is the natural frequency of the second order system, ζ_n is the damping ratio, and k is a constant gain. The natural frequency ω_n is chosen to be larger than the frequency at which the spatial filtering occurs, in this case about 2.5 kHz, so that rate feedback is applied to all the observable modes of the system. Above ω_n, the control law rolls off fast enough that the loop gain, $G_{yu}(s)K(s)$, rolls off. For these frequencies, the phase of the controller goes to –90 degrees. Normally, this would be unacceptable for a collocated system. In this case, however, the phase of the transfer function $G_{yu}(s)$ is near 0 degrees above 2.5 kHz, so that the phase of the loop gain will be acceptable. The output of the PVDF sensors was also measured in order to assess the effectiveness of the closed-loop control in reducing the structural strain.

The chosen control law was simultaneously applied to each PVDF-PZT pair separately, without taking into consideration the interaction between loops. This *independent loop closure* is expected to work well, because rate feedback is stabilizing for collocated structural control, even with multiple sensor/actuator pairs.

The behavior of the system was compared with and without feedback control, and with a disturbance driving the system, to determine the effectiveness of the control system. The upper plot in Figure 29 shows the autospectra of PVDF sensor number 1 on panel 1, with and without feedback control. The open-loop spectrum is plotted in gray, while the closed-loop spectrum is plotted in black. The bottom plot is the ratio of the open-loop and closed-loop spectra, expressed in decibels. The closed-loop response is reduced by as much as 20 dB near 1000 Hz, and by more than about 10 dB near 1500 Hz. Further, the reduction is greater than 0 dB over the entire range from 0-2000 Hz, except for a small frequency range near 1750 Hz. Thus, it appears the controller is damping the panel structural modes over a wide range of frequencies.
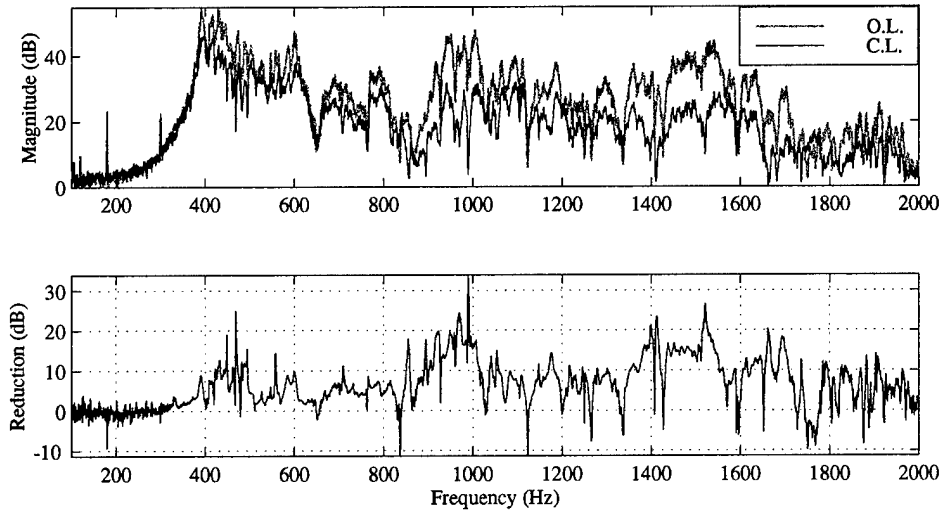
Figure 29: Comparison of open-loop and closed-loop strain autospectra for panel 1, location 1.

The effectiveness of the control action in reducing acoustic behavior inside the test-bed was tested using three microphones, located behind panel 2. Figure 30 shows a comparison of the open-loop and closed-loop acoustic pressure autospectra. The open-loop response is indicated by the gray curve, and the closed-loop response is represented by the black curve. The reduction in sound levels is 8 dB around 400 Hz, 15 dB at 820 Hz, and 7 dB at 950~Hz. Again, the performance was

quantified by integrating the sound pressure spectra from three microphones over 100 Hz frequency bands, as shown in Figure 31. The controller reduced the acoustic pressure in most frequency bands, although not as effectively as for structural strain. The maximum reduction is about 3 dB, and occurs between 900 Hz and 1000 Hz. Although this level of noise reduction is low, we note that only six of sixty panels were controlled. We expect that much better performance would result if more panels were controlled.

Figure 30: Comparison of open-loop and closed-loop acoustic pressure autospectra for a microphone located behind panel 2.

Figure 31: Comparison of open-loop and closed-loop acoustic pressure autospectra integrated in 100 Hz frequency bands.

Narrowband Feedback Control

Reconfigurable arrays are arrays of discrete actuator or sensor elements with a weighting that is tuned to target individual modes. Multiple different weighting vectors can be u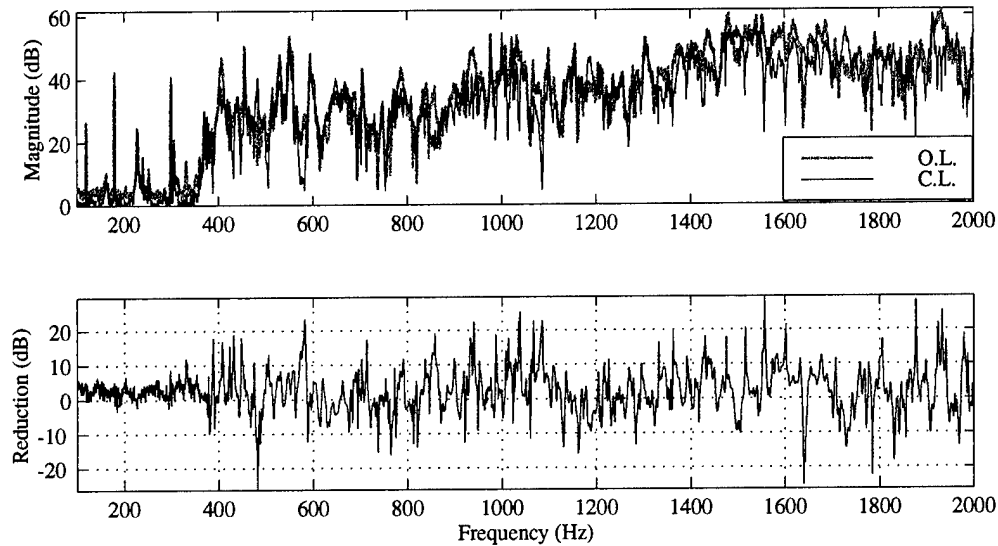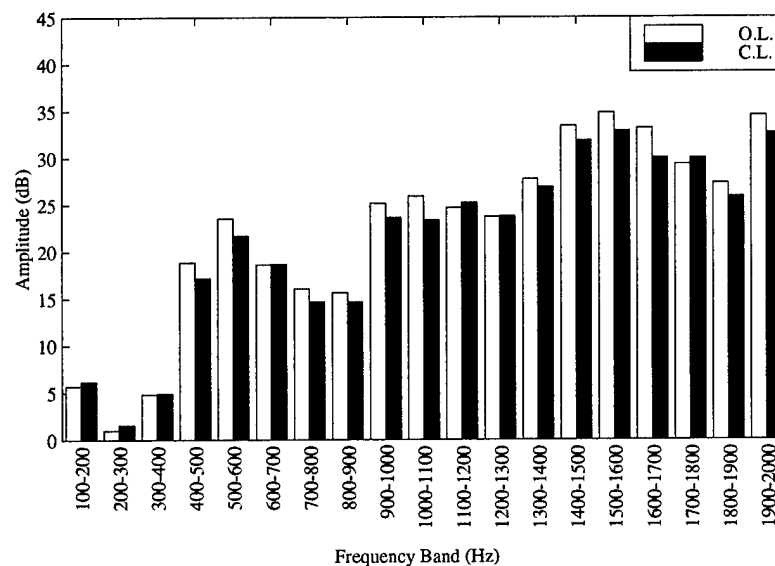sed so that multiple modes can be isolated from the same array elements. The weighting can be updated to track the modes as the system changes Figure 32.
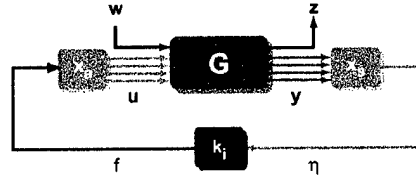

Figure 32: The weights on the sensor array, x_s, serve as a serve as a filter to the sensors signals y, while the weights on the actuator array, x_a, serves as a filter to the actuator signals u. The weighted signals, η and f can be designed to be modal signals, which allows for the design of simpler controllers, k_i.

The goal of reconfigurable arrays is to enable the design of reduced-order controllers for complex structures, improve closed-loop robustness and broaden the region of good performance in the presence of plant uncertainty. The key to reconfigurable arrays lies in determining the optimal weighting for the sensor and actuator elements. The optimal weights are those that map a single mode from forcing to measurement acting as pre- and post- filters to the control algorithm, allowing the implementation of reduced-order controllers (Figure 32).

There are various ways to compute the weighting vectors. On structures with simple boundary conditions and low damping the weights can be the real part of the residues of the desired modes evaluated at the sensor locations (in this case, $x_s = x_a$). Another alternative, also valid when $x_s = x_a$, is to invert the transfer function matrix, so that the weighting vectors are given by:

$$x_s = (G_{yu}^T G_{yu})^{-1} G_{yu}^T f_d,$$

where G_{yu} is the matrix of measured transfer functions from actuators, u to sensors, y, and f_d is the desired frequency response of the weighted signal. In this case the weights will be complex in systems with non-zero damping and, therefore, difficult to implement experimentally.

A more general approach is to minimize a cost function that represents the inverse of a performance metric. Consider the transfer function matrix G_{yu}, given by

$$y = G_{yu} u.$$

The array weights on the actuators and sensors create a weighted sensor response, η, and a weighted actuator input, f, according to:

$$\eta = x_s^T y \quad \text{and} \quad u = x_a f.$$

Note that the weighting vectors are not necessarily identical. Using the equations above, a transfer function from the weighted actuators to the weighted sensors,

$$\eta = x_s^T G_{yu} x_a f,$$

can be defined. When targeting multiple modes for control, x_s and x_a become matrices that, when properly chosen, render the weighted transfer function matrix diagonal, mapping modal excitation to modal response. Cost functions were designed to minimize the modal response of unwanted modes,

R_n, while maximizing the residue of the desired mode, R_m, in the weighted transfer function x_s^T G_{yu} x_a. The H_2, H_∞ and H_{mimo} cost functions used were:

$$H_2 = \frac{\sum_n R_n^* R_n}{R_m^* R_m} \quad , \quad H_\infty = \frac{\max_n R_n^* R_n}{R_m^* R_m} \quad , \quad H_{mimo} = \frac{\left\| G_{yu} x_a x_s^T \right\|_{\omega \in n}}{\left\| G_{yu} x_a x_s^T \right\|_{\omega \in m}} \quad ,$$

where $*$ indicates the complex conjugate, $\omega \in n$ represents the frequency points where the weighted response should be minimized and $\omega \in m$ represents the frequencies of the modes of interest. These cost functions can also include penalty terms if the weighted plant, x_s^T G_{yu} x_a, does not have collocated behavior or does not roll-off with increasing frequency.

$$k(s) = \left(\frac{s - \omega_c}{s^2 + 2\zeta_c \omega_c s + \omega_c^2} \right) \prod_i \left(\frac{g_i \omega_i^2}{s^2 + 2\zeta_i \omega_i s + \omega_i^2} \right)$$

The controllers used in the experiments consist of the combination of positive-position feedback (PPF) controllers in series with a stabilized integrator. The controller variables were the low frequency corner, ω_c, the damping ratio of the low frequency corner, ζ_c, the damping ratio at the target frequencies, ζ_i, the gains, g_i, and the target frequencies of each mode, ω_i. Controllers with the form shown above have been experimentally implemented in a dSPACE real-time controller, sampling at 10 kHz with a 50-1000 Hz broadband random acoustic disturbance. A typical results in shown in
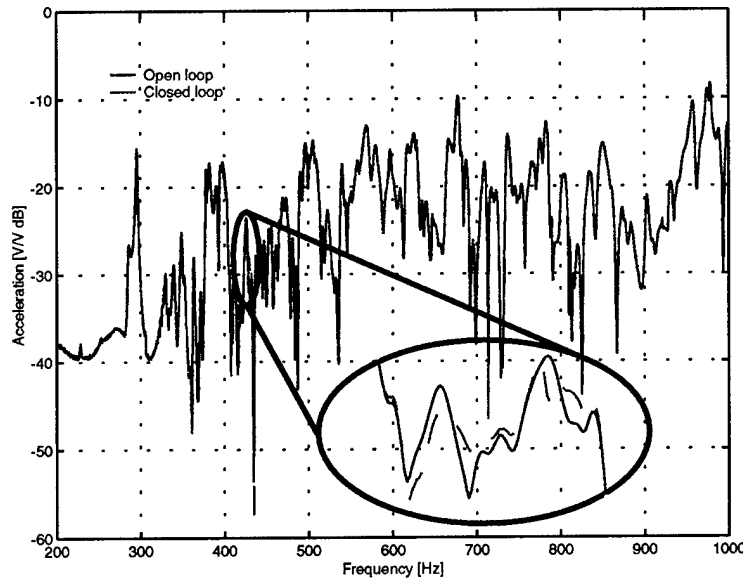
Figure 33: Comparison between open- and closed-loop responses obtained from an array of accelerometer sensors and PZT actuators. The controller was designed to target the mode at 426 Hz, yielding a 4 dB reduction in the acceleration. Open and closed-loop responses are identical outside the band shown above.

Summary

Multiple collocated sensor/actuator (PVDF-PZT) pairs were used to damp the structural modes of a model fuselage, designed to be representative of aircraft structures. Active plies with these sensor/actuator pairs were manufactured and bonded on the structure. Strain rate feedback was

applied to each pair independently and closed-loop control reduced the structural acceleration as much as 20 dB and interior acoustic pressure level as much as 10 dB at some resonant peaks. Similarly, reduced-order narrowband controllers were designed using arrays of sensors and actuators. The performance measures presented here were obtained with less than 10% of the test-bed being instrumented. Instrumentation of a greater portion of the test-bed is expected to produce greater reduction in the structural acceleration and interior noise level.

3. PUBLICATIONS

Ghandi, K. and N.W. Hagood, "Nonlinear Finite Element Modeling of Phase Transitions in Electro-Mechanically Coupled Material", *Proceedings of SPIE's Symposium on Smart Structures and Materials*, pp. 121-140, San Diego, CA, 1996.

Yung, J., "Compensation Methodologies for Local Control Using Strain Actuators and Sensors", *S.M. Thesis - AMSL Report 96-2*, Massachusetts Institute of Technology, Cambridge, MA, August 1996.

Heremans, C., Wordsworth, S., Lee, J.H., Kucera, J.P, Chiang, Y.M., and H.L. Tuller, "New Potential Material Candidates for High Strain Actuators", *Materials Research Society 1996 Fall Meeting*, Advances in Materials for Smart Systems - Fundamentals and Applications, Boston, MA, Dec 2-6, 1996.

Ghandi, K., N.W. Hagood, "A hybrid finite element model for phase transitions in nonlinear electro-mechanically coupled material", *Proceedings of SPIE's 4th Annual Symposium on Smart Structures and Materials*, pp. 97-112, San Diego, CA, 1997.

Fripp, Michael L.R., Donald Q.O'Sullivan, S.R. Hall, N.W. Hagood, K. Lilienkamp, "Test-bed design and modeling for aircraft interior acoustic control", *Proceedings of SPIE's 4th Annual Symposium on Smart Structures and Materials*, pp. 88-99, San Diego, CA, 1997.

Warkentin, David J., Nesbitt W. Hagood, "Nonlinear piezoelectric shunting for structural damping", *Proceedings of SPIE's 4th Annual Symposium on Smart Structures and Materials*, pp.747-757, San Diego, CA, 1997.

Pizzochero, Alessandro, "Residual actuation and stiffness properties of piezoelectric composites: theory and experiment", *S.M. Thesis*, Massachusetts Institute of Technology, Cambridge, MA, September 1997.

Rosenthal, Matthew E., "Ceramic Microforming Process" *S.M. Thesis*, Massachusetts Institute of Technology, Cambridge, MA, 1997.

Ghandi, Kamyar, "Nonlinear Modeling and Characterization Techniques for Phase Transition in Electromechanically Coupled Devices", *Ph.D. Thesis - AMSL Report 98-1*, Massachusetts Institute of Technology, Cambridge, MA, May 1998.

O'Sullivan, Donald Q., "Aircraft Interior Structural-Acoustic Control Design", *S.M. Thesis - AMSL Report 98-2*, Massachusetts Institute of Technology, Cambridge, MA, May 1998.

Bingham, Brian S., "Structural-Acoustic Design and Control of an Integrally Actuated Composite Panel", *S.M. Thesis - AMSL Report 98-5*, Massachusetts Institute of Technology, Cambridge, MA, September 1998.

Y.-M. Chiang, G.W. Farrey, A.N. Soukhojak, S.A. Sheets, "Growth and Characterization of Alkaline Bismuth Titanate Single Crystal Piezoelectrics," Proceedings of the 9th US-Japan Seminar on Dielectric and Piezoelectric Ceramics, Nov. 3-5, Okinawa, Japan.

Y.-M. Chiang, G.W. Farrey, and A.N. Soukhojak, "Lead-Free High Strain Single Crystal Piezoelectrics," *Appl. Phys. Lett.*, **73**[25] 3683-3685 (Dec, 1998).

Bingham, Brian S., Nesbitt W. Hagood and Mauro J. Atalla, "Performance comparison of feedback and feedforward structural-acoustic control techniques", *SPIE Conference on Smart Structures and Integrated Systems*, pp. 222-234, Newport Beach, CA, USA, March 1999.

Yung, J.H. and E.F. Crawley, "Compensation methodologies for local control using strain actuators and sensors," *SPIE Conference on Mathematics and Control in Smart Structures*, pp 913-924, Newport Beach, CA, USA, March 1999.

G.W. Farrey, A.N. Soukhojak, S. Sheets, and Y.-M. Chiang, "Growth and Characterization of $Na_{1/2}Bi_{1/2}TiO_3$-$K_{1/2}Bi_{1/2}TiO_3$-$BaTiO_3$ Single Crystal Piezoelectrics," *IEEE International Symposium on Applications of Ferroelectrics*, 24-27 Aug. 1998, Montreux, Switzerland (ISBN 0-7803-4959-8), June 1999, pp. 551-554.

Fripp, Michael L., Mauro J. Atalla, Nesbitt W. Hagood, Cagri Savran and Steve Tistaert, "Reconfigurable arrays for broadband feedback control of aircraft fuselage vibrations", *Proceedings of the 10th International Conference on Adaptive Structures and Technologies–ICAST*, pp. 447-456, Paris, France, October 1999.

J.-H. Lee and Y.-M. Chiang, "Pyrochlore-Perovskite Transformation in Highly Homogeneous (Pb,La)(Zr,Sn,Ti)O_3 Powders," *J. Mater. Chem.*, **9**, 3107-3111 (1999).

Heremans, C. and H.L. Tuller, "Lead Hafnate Zirconate Titanate-based Perovskite Materials for Acuatation", *J. Euro.Ceram. Soc.*, 19, pp. 1133-1137, 1999.

Tupper, Malinda M. and Matthew E. Rosenthal, "Microprocessing of Piezoelectric Fibers", Poster presented at *the 101st Annual American Ceramic Society Meeting,*

Peter S. Lively, "Dynamic shape estimation using Kalman filtering", *S.M. Thesis - AMSL Report 00-1*, Massachusetts Institute of Technology, Cambridge, MA, January 2000.

Gregory W. Farrey, *Dielectric and Electromechanical Properties of Alkaline Bismuth Titanate Single Crystals*, S.M. Thesis, MIT, February 2000.

Lin, Ching-Yu and N.W. Hagood, "Compression depolarization of PZT piezoelectric materials under high electromechanical driving levels", *Proceedings of the SPIE Conference on Active Materials: Behavior and Mechanics*, pp. 114-125, Newport Beach, CA, USA, March 2000.

Savran, Cagri A., Mauro J. Atalla and Steven R. Hall, "Broadband active structural-acoustic control of a fuselage test-bed", *Proceedings of the SPIE Conference on Mathematics and Control in Smart Structures*, pp. 136-147, Newport Beach, CA, USA, March 2000.

Fripp, Michael, Mauro J. Atalla and Nesbitt W. Hagood, "Reconfigurable arrays of collocated sensors and actuators for modal isolation", *Proceedings of the SPIE Conference on Mathematics and Control in Smart Structures*, pp. 540-552, Newport Beach, CA, USA, March 2000.

Lively, Peter S., Mauro J. Atalla and Nesbitt W. Hagood, "Dynamic shape estimation using Kalman filtering", *Proceedings of the SPIE Conference on Smart Structures and Integrated Systems*, pp. 521-532, Newport Beach, CA, USA, March 2000.

Fripp, Michael L., "Reconfigurable arrays of collocated sensors and actuators for modal isolation and feedback control", *Ph.D. Thesis - AMSL Report 00-5*, Massachusetts Institute of Technology, Cambridge, MA, June 2000.

Savran, Cagri, "Broadband active structural-acoustic control of a fuselage test-bed", *S.M. Thesis - AMSL Report 00-7*, Massachusetts Institute of Technology, Cambridge, MA, June 2000.

Atalla, Mauro J., Michael L. Fripp, Jeremy H. Yung, and Nesbitt W. Hagood, "Design of Reduced-Order Controllers on a Representative Aircraft Fuselage", to appear in the Proceedings of the *IUTAM Smart Structures and Structronic Systems Symposium*, Magdeburg, Germany, September 2000.

Heremans, C. and H.L. Tuller, "Field-induced Antiferroelectric-Ferroelectric Phase Transitions in the $Pb_{0.98}La_{0.02}(Zr_{0.70}Hf_{0.30})_{1-x}Ti_xO_3$ System," *J. Appl. Phys.*, pp. 87:3, 1458-1486, 2000.

Fripp, Michael and Mauro J. Atalla, "A review of modal sensing and actuation techniques", *Shock and Vibration Digest Journal*, 33(1), 3-14, 2001.

J.-H. Lee and Y.-M. Chiang, "Pressure-Induced Pyrochlore-Perovskite Phase Transformation in PLZST Ceramics," *J. Electroceramics*, 6[1] 7-12 (2001).

Bingham, B., M.J. Atalla and N.W. Hagood, "Comparison of structural-acoustic control designs on an active composite panel", to appear in *Journal of Sound and Vibration*.

Lively, Peter S., Mauro J. Atalla and Nesbitt W. Hagood, "Dynamic shape estimation using Kalman filtering", to appear in *Smart Materials and Structures*.

Atalla, Mauro, J.S. Lederle, J.H. Yung, "Design of a Reduced-Order Structural-Acoustic Controller on a Representative Aircraft Fuselage," in preparation to be submitted to the *Journal of the Acoustical Society of America*.

Gregory W. Farrey, *Dielectric and Electromechanical Properties of Alkaline Bismuth Titanate Single Crystals*, S.M. Thesis, MIT, February 2000.

4. PERSONNEL

4.1 FACULTY

Chiang, Yet-Ming
Cima, Michael J

Crawley, Edward F
Hobbs, Linn Walker
Hagood, Nesbitt W
Hall, Steven R
Tuller, Harry L

4.2 SCIENTIFIC STAFF

Atalla, Mauro J
Bauer, Paul H
Centorino, John A
Heremans, Catherine
Kane Jr., John J
Lee, Joon-Hyung
Liberatore, Michael J
Rigione Jr., Leonard J
Robertson, David
Rosenthal, Mathew
Spears, Mareme
Wang, Haifeng
Warkentin, David
Yu, Taehwan

4.3 GRADUATE STUDENTS

Avrahami, Ytshak
Bingham, Brian – MSc in Mechanical Engineering
Chan, Kin
Dunn, Christopher – MSc in Mechanical Engineering
Farrey, Gregory W
Fripp, Michael – MSc and PhD in Aeronautics and Astronautics
Ghandi, Kamyar – PhD in Aeronautics and Astronautics
Glenn, Timothy
Harper, John E – MSc in Aeronautics and Astronautics
Janos, Benon
Kershner, Ryan J
Lederle, Stephane
Liberatore, Michael
Lin, Ching-Yu
Lively, Peter S – MSc in Aeronautics and Astronautics
O'Sullivan, Donald – MSc in Mechanical Engineering
Pizzochero, Alessandro – MSc in Aeronautics and Astronautics
Prechtl, Eric – MSc and PhD in Aeronautics and Astronautics
Pulitzer, Seward – MSc in Aeronautics and Astronautics
Rodgers, John P – MSc and PhD in Aeronautics and Astronautics
Rosenthal, Mathew – MSc in Materials Science Engineering
Savran, Cagri – MSc in Mechanical Engineering
Shin, Sangjoon – MSc in Aeronautics and Astronautics
Song, Kyungyeol
Tupper, Malinda M
Tzianetopoulou, Theodora – MSc in Aeronautics and Astronautics
Yung, Jeremy – MSc in Aeronautics and Astronautics

4.4 UNDERGRADUATE STUDENTS

Adilstam Fredrik
Berkowski, George P
Booher, Timothy B
Bower, Nathaniel
Chuang, Yuan Luen
Coulter, Eric A
Diaz, Patricia
Faiz, Jeehan S
Fan, Winston
Garcia, Christian D
Hohnson, Jaymee L
Klicka, Matt M
Krawczyk, Jodi L
Kucera, John-Paual
Kwon, Daniel W
Lewis, Alexis
Maskaly, Garry R
Matuszeski, Adam J
Mohamed, Farzana S
Olazabal, Carmen M
Prazan, Aaron R
Rinderknecht, Derek G
Tistaert, Stephen
Torres, Joel
Uebelhart, Scott A
Vidanage, Sean N
Wordsworth, Shelley L
Yu, Tae-Hwan
Ziskin, Matt J

5. PATENTS

"Piezoelectric Actuators and Methods of Making Same" by Y.-M. Chiang, G.W. Farrey, N.W. Hagood IV, Andrey N. Soukhojak, Haifeng Wang, Application No. 09/174,981, October 1998.

"Rhombohedral-Phase Barium Titanate as a Piezoelectric Transducer", by H.L. Tuller.

"Electromechanical and Photoelectrochemical Methods for Etching Silicon Carbide" by R. Mlcak and H.L. Tuller.